Multi-scale modeling of proton exchange membrane fuel cell by coupling finite volume method and lattice Boltzmann method

Li Chen, Yong-Liang Feng, Chen-Xi Song, Lei Chen, Ya-Ling He, Wen-Quan Tao *

Key Laboratory of Thermo-Fluid Science and Engineering of MOE, School of Energy and Power Engineering, Xi'an Jiaotong University, Xi'an, Shaanxi 710049, China

ARTICLE INFO

ABSTRACT

A multi-scale modeling framework combining finite volume method (FVM) and lattice Boltzmann method (LBM) previously developed by our group is used to predict electrochemical transport reaction in proton exchange membrane fuel cell (PEMFC) cathode with a parallel gas channel (GC), a gas diffusion layer (GDL) with porous structures and a catalyst layer (CL) with idealized microstructures. In this framework, the PEMFC cathode is divided into two sub-domains, one is GC and the other contains GDL and CL. The FVM is used to simulate transport phenomena in the GC sub-domain, while the LBM is employed for pore-scale transport phenomena in the GDL and CL as well as proton conduction in the CL in the other sub-domain. Two reconstruction operators are adopted to transfer macro density, velocities and concentration in the FVM to density distribution functions and concentration distribution functions in the LBM at the interface between the two sub-domains. Simulation results show that the coupled (hybrid) simulation strategy developed is able to predict transport phenomena in the GC and to capture the pore-scale transport processes in porous GDL and CL. In addition, some techniques to save the computational resources and to improve the efficiency of the coupled (hybrid) simulation strategy are discussed.

© 2013 Elsevier Ltd. All rights reserved.

1. Introduction

Proton exchange membrane fuel cell (PEMFC) has been considered as an alternative power source for various applications and has received much attention during the past decades, due to its advantages including high power density, low operation temperature, high efficiency, low emissions and low noise. A typical PEMFC consists of the following components with different length scales: bipolar plates, gas channels (GC) curved in bipolar plates, gas diffusion layers (GDL), catalyst layers (CL) and proton exchange membrane (PEM) sandwiched between anode and cathode. Correspondingly, transport phenomena involved in these components show the characteristics of multi-scale and should be considered at different length scales [1]. For example, reactants flow into the GC with dimensions of centimeters, permeate into porous GDL with mean pore size of tens of micrometers, finally diffuse into porous CL with pore size ranging from a few tens of nanometers to a few micrometers where electrochemical reaction occurs.

Modeling and simulation have been used extensively during the past years to investigate coupled phenomena of fluid flow, mass, heat and the electric charge transfer in PEMFC. Recently, high-performance computing and advanced numerical methods have enabled researchers to numerically study such nonlinear coupled multi-scale transport processes in PEMFC as well as individual components with higher fidelity. Based on whether the actual morphology of porous components (GDL, CL and PEM) in PEMFC is considered explicitly, modeling and simulation of PEMFC can be divided into two major categories: macro-scale models solving the volumetric averaging of conservation equations in each elementary volume assuming a homogeneous porous components with isotropic or anisotropic transport properties; and pore-scale models incorporating realistic or approximately realistic microstructures of porous components. A brief review of the two kinds of models is presented as follows.

There have been extensive studies using macro-scale models to predict hydrodynamics mechanism and electrochemical reactions in PEMFC. The macro-scale models based on the continuity assumptions numerically solve a set of conservation equations including mass, momentum, energy, species and ionic and electronic charges with appropriate boundary and initial conditions, using conventional computational fluid dynamics (CFD) method such as finite volume method (FVM) and finite element method (FEM). With the help of a group of empirical and constitutive relationships as well as kinetic equations for electrochemical reaction, such macroscopic models have been providing full image of operating processes taking place in PEMFC. More and more comprehensive

* Corresponding author. Tel./fax: +86 29 82669106.
   E-mail addresses: dandaoxingtianya@163.com (L. Chen), feng.2k9@stu.xjtu.edu.cn (Y.-L. Feng), song.chenxi@stu.xjtu.edu.cn (C.-X. Song), chenlei.09@stu.xjtu.edu.cn (L. Chen), yalinghe@mail.xjtu.edu.cn (Y.-L. He), wqtao@mail.xjtu.edu.cn (W.-Q. Tao).

Nomenclature

a, b	length	β_n	variables in Eq. (37)
$\mathbf{c}$	lattice speed	ε	knudsen number porosity
c_s	lattice sound speed	ϕ	variable
C	concentration	r_c	cathode concentration dependence
Da	Damkömohler number	η	over-potential
D	diffusivity	v	kinematic viscosity
f	density distribution function	ρ	density
F	Farady constant	σ	proton conductivity
g	concentration distribution function	τ	relaxation time
h	potential distribution function	ω	weight factor
H	height	Γ	nominal diffusion coefficient
I	current density		
l_0	length scale		
L	length	*Superscript*	
J	specially chosen constant in Eq. (10)	eq	equilibrium
k	reaction rate in Eq. (36)		
K	specially chosen constant in Eq. (10)		
$\mathbf{n}$	normal vector	*Subscript*	
N_n	variables in Eq. (37)	A	species A
R	gas constant	e	electrolyte
S	stress tensor	g	gas
t	time	i	direction of the lattice velocity
t_0	time scale	in	inlet
T	temperature	k	kth component
$\mathbf{u}$	velocity vector	L	lattice unit
u,v	velocities along in x, y directions	n	nitrogen
x, y	cartesian coordinates	o	oxygen
Δx	space step	P	physical unit
Δt	time step	ref	reference
ε	small expansion parameter	α,β,γ	coordinate direction indexes
α	transfer coefficient	w	water vapor

macro models, from initial one-dimensional models [2–4] to complex three-dimensional two-phase models [5,6], have been developed to profoundly understand multi-scale and multiple physicochemical transport phenomena in PEMFC, among which the multiphase mixture model [7] and multi-fluid multi-phase model [8] are the most famous. Recently, a general model coupling mass, charge, momentum, energy transport and particularly liquid water dynamic behaviors was developed by Le and Zhou [9]. This model can predict the liquid water dynamics in the GC, GDL and CL and reveal the effects of liquid water distributions on the distributions of flow field, temperature, concentration and current density. Overall, macro-scale models, with the advantage of computational efficiency, play prominent roles in understanding transport processes in PEMFC. A complete review of literatures using macro-scale models is beyond the scope of this paper and more details can be found in [10].

Several components in PEMFC, including GDL, CL, PEM and sometimes micro pore layer (MPL), are porous medium. Commonly, the GDL is carbon fiber based porous media such as carbon paper and carbon cloth. It shows complex structures with heterogeneous characteristics which concretely present as heterogeneous porosity, wettability, effective diffusivity and permeability [11]. Macro-scale models mentioned above, although allow computationally efficient larger scale simulations, usually neglect the influence of porous structures and related heterogeneous characteristics of GDL because the averaged length of a computational element in macro-scale models is much larger than typical pore size of GDL. Due to such ignorance, macro-scale models have to employ several flow empirical relations expressing the relationship between macroscopic transport properties (such as effective diffusivity, permeability) and macroscopic structural parameters (such

as porosity and tortuosity), for example, relation between permeability and porosity and that between effective diffusivity and porosity. The accuracy of some of these empirical relations applied to GDL materials is questionable and these relations sometimes predict unreasonable distributions in the porous components [12], thus they still need further validation. MPL, CL and PEM also show the similar heterogeneous characteristics as GDL, and macro-scale models also do not resolve the realistic structures of these porous components. Thus, macro-scale models simulating these components suffer the same problems encountered in modeling GDL.

Pore-scale models directly describe the transport processes in porous media based on the realistic structures and thus do not need the relative macroscopic transport properties. They can be used to improve the fundamental understanding of the reactive transport in porous components of PEMFC. The pore-scale studies can be broadly categorized into rule-based and first-principle-based models [13]. Rule-based models, such as pore-network (PN) modeling approaching, use a somewhat idealized network to represent the porous medium. PN partly considers the porous morphology of GDL by constructing the GDL as a regular cubic network of pores connected by throats, and in each pores and throats, simplified hydrodynamic and reactive equations are solved. Recently, several studies adopting this method have been reported to investigate effects of GDL structures on liquid water distribution [12], to obtain the GDL specific capillary pressure versus saturation correlation [14] and to acquire liquid water transient distribution in GDL [15]. Because of the topologically and geometrically idealized structures used and the simplified hydrodynamics considered, PN do not always fully account for the pore-scale processes occurring in realistic porous media.

The first-principle-based methods resolve the underlying transport processes by solving the governing equations, namely the Navier–Stokes equations. The governing equations can be solved by either "top-down" approach or "bottom-up" approach. The conventional numerical methods such as FVM fall into the "top-down" approach category, while the lattice Boltzmann method (LBM) and molecular dynamics (MD) belong to the "bottom-up" approach [13]. Among these pore-scale modeling using top-down CFD methods, FVM-based commercial software FLUENT is widely used [16–19]. The general procedures using this software are as follows: constructing the microstructures of the porous components; meshing the microstructures using mesh generation software; and finally importing the meshes into FLUENT to solve related conservation equations. Recently, Park et al. [16] constructed the GDL by randomly placing impermeable cylinders and studied the processes of liquid water removal from the GDL with different GDL contact angle and driving pressure. Wang et al. [17,18] simulated the oxygen and charge transport in CL with regular and random microstructures and later they further simulated transport and reaction in CL with real CL structures reconstructed using stochastic method [19]. The major difficulty encountered in pore-scale models using top-down CFD methods is the discretization, namely the grid generation, of the porous media. Actually, grid generation of porous media, the quality of which significantly affects the convergence, stability and accuracy of subsequent numerical simulations, is not very successful due to irregular regions usually presenting high tortuosity and distortion in porous media. Fortunately, bottom-up numerical methods such as LBM and MD have the inherent capacity of accounting for the porous structures due to their remarkable ability of treating complex boundaries. There have been an increasing number of studies adopting LBM to investigate the transport processes and structural properties in GDL [20–23]. Park et al. [20] simulated the motion and break-up of a liquid droplet subject to air flow in a two dimensional GDL with actual porous structures. Mukherjee et al. [22] investigated the effects of porous structures on liquid water transport process. Liang and Cheng [21] explored the effect of GDL wettability on liquid water transport and distribution. Chen et al. [23] investigated the dynamic behaviors of liquid water suffered to the air flow in GDL under interdigitated GC. Currently, using LBM to predict coupled reactive transport phenomena in CL is a challenge work. Kim and Pitsch [24] adopted LBM to simulate the transport of oxygen and protons through a constructed CL represented by carbon spheres surrounded by an ionomer film. In addition, MD has also been used to predict transport phenomena and structural characteristics of the PEM [25,26].

From the above reviews, it can be found that macro-scale models are computationally efficient and can handle large scale simulations, but they heavily rely on phenomenological descriptions of fluid flow and transport processes and require effective macroscopic transport properties of the porous components, and thus they cannot resolve local transport details within the porous components. Pore-scale models, especially those using bottom-up numerical methods, can capture the fundamental pore-scale details of transport processes, but require large and even prohibitive computational resources and thus are limited to a small fraction of the porous components. Therefore, simulation strategies that combining the merits of macro-scale and pore-scale models while avoiding the disadvantages of each are currently required to be developed to simulate multi-scale transport phenomena in PEMFC. Of particular interest is regionally coupling the FVM macro-scale model with LBM pore-scale model, which requires information exchange between the fluid variables in the macro-scale model and the distribution functions in the LBM.

The author's group has done some preliminary work regarding such subject by using a coupled simulation strategy [27,28]. In this strategy, instead of pursuing a single uniform numerical method for the entire domain, different numerical methods (or models) are used to predict transport process in different local regions and information is exchanged at the interfaces between neighboring regions. During the implementation of such strategy, the computational domain is divided into several sub-domains and in each sub-domain the appropriate numerical method corresponding to the transport processes in this sub-domain is applied. For example, when simulating transport processes in PEMFC using such coupled modeling strategy, a PEMFC can be divided into four sub-domains, namely, GC, GDL, CL and PEM. Then, FVM can be used for simulating transport processes in GC, LBM for that in GDL, LBM or MD for that in CL, and MD for that in PEM. Therefore, advantages of different numerical methods are fully used, leading to the resolution of pore-scale details of transport processes in complex porous components with acceptable computational cost. Currently, this coupled simulation strategy is experiencing a rapid growth in the modeling of multi-scale problems. The critical task and major difficulty in the coupled stimulation strategy is how to exchange information at the interface of neighboring subdomains, or essentially between different numerical methods [27]. Recently the author's group has done much work on the coupled simulation strategy by coupling different methods: FVM and LBM [29–32], FVM and MD [33] and FVM and direct-simulation Monte Carlo method (DSMC) [34].

In a previous study, we conducted some preliminary simulations on the transport processes in cathode side of PEMFC by using the coupling FVM and LBM [31]. In that study, that GC and GDL were considered while CL was treated as an ultra thin interface; and only fluid flow, mass transport and chemical reaction were involved without taking into account the conduction of irons. In the present study, we go on further to demonstrate the implementation of the coupled stimulation strategy to simulate transport processes in PEMFC cathode, where the porous structures of CL are considered and the transport process of protons is involved. Besides, the using of coarse-fine grid system is evaluated and factors affecting the maximum grid ratio available are discussed. The rest of this paper is arranged as follows. First, FVM and LBM involved are briefly introduced in Section 2 and the coupled scheme between FVM and LBM is described in Section 3. Section 4 presents the validation of the multi-scale coupled simulation scheme. Then, the coupled simulation scheme is applied to simulate the fluid flow, multi-component species and proton transport and electrochemical reaction in PEMFC cathode side in Section 5. Finally, some conclusions drawn from this work are given in Section 6.

2. LBM and FVM

2.1. Brief introduction to LBM

Due to its excellent numerical stability and constitutive versatility, the LBM has developed into an alternative and promising numerical approach for simulating fluid flow in recent years and is particularly successful in applications involving interfacial dynamics and complex geometries [35,36]. LBM simulates pseudo-fluid particles on a mesoscopic level based on Boltzmann equation using a small number of velocities adapted to a regular grid in space. The obvious advantages of LBM are the simplicity of programming, the parallelism of the algorithm and the capability of incorporating complex microscopic interactions. For simplicity, only brief introductions for fluid flow, species transport and proton conduction LB models are given in the following paragraphs.

2.1.1. LB model for fluid flow

The LB fluid flow model employed is based on the simple and popular Bhatnagar–Gross–Krook (BGK) method [37]. DnQb lattice

is adopted where n denotes the dimension and b represents number of discrete velocities [38]. The evolution of LB equation is described by

$$f_i(\mathbf{x} + \mathbf{c}_i\Delta t, t + \Delta t) - f_i(\mathbf{x}, t) = -\frac{1}{\tau_v}(f_i(\mathbf{x}, t) - f_i^{\text{eq}}(\mathbf{x}, t)) \tag{1}$$

where $f_i(\mathbf{x}, t)$ is the particle distribution function with velocity $\mathbf{c}_i$ at the lattice site x and time t, $f_i^{\text{(eq)}}$ is the ith equilibrium distribution function, Δt is the time increment, and τ is the collision time. $\mathbf{c}_i$ is the discrete velocities. For D2Q9 model in this study, $\mathbf{c}_i$ is given by

$$\mathbf{c}_i = \begin{cases} 0 & i = 0 \\ \left(\cos\left[\frac{(i-1)\pi}{2}\right], \sin\left[\frac{(i-1)\pi}{2}\right]\right) & i = 1,2,3,4 \\ \sqrt{2}\left(\cos\left[\frac{(i-5)\pi}{2} + \frac{\pi}{4}\right], \sin\left[\frac{(i-5)\pi}{2} + \frac{\pi}{4}\right]\right) & i = 5,6,7,8 \end{cases} \tag{2}$$

The equilibrium distribution function is given by

$$f_i^{\text{eq}} = \omega_i \rho \left[1 + \frac{3}{c^2}(\mathbf{c}_i \cdot \mathbf{u}) + \frac{9}{2c^4}(\mathbf{c}_i \cdot \mathbf{u})^2 - \frac{3}{2c^2}u^2\right] \tag{3}$$

where the weights ω_i=4/9, $i = 0$; ω_i=1/9, i = 1,2,3,4; ω_i=1/36, i = 5,6,7,8. Fluid density ρ and velocity u can be obtained from the first and second moments of the particle distribution functions

$$\rho = \sum_i f_i \tag{4}$$

$$\rho\mathbf{u} = \sum_i f_i \mathbf{c}_i \tag{5}$$

The kinematics viscosity in lattice unit is related to the collision time by

$$v = c_s^2(\tau_v - 0.5)\Delta t \tag{6}$$

Through Chapman–Enskog expansion, Eqs. (1) and (3) lead to the continuity and the Navier–Stokes equations near the incompressible limit

$$\frac{\partial \rho}{\partial t} + \nabla \cdot (\rho\mathbf{u}) = 0 \tag{7}$$

$$\rho\left[\frac{\partial \mathbf{u}}{\partial t} + (\mathbf{u} \cdot \nabla)\mathbf{u}\right] = -\nabla p + \nabla \cdot [\rho\mu(\nabla\mathbf{u} + \nabla\mathbf{u}^{\text{T}})] \tag{8}$$

2.1.2. LB model for species transport

The following evolution of LB equation is used to describe species transport [39]

$$g_{i,k}(\mathbf{x} + \mathbf{c}_i\Delta t, t + \Delta t) - g_{i,k}(\mathbf{x}, t) = -\frac{1}{\tau_{D,k}}(g_{i,k}(\mathbf{x}, t) - g_{i,k}^{\text{eq}}(\mathbf{x}, t)) \tag{9}$$

where $g_{i,k}$ is the concentration distribution function of kth component in the direction i. The equilibrium concentration distribution function $g_{i,k}^{\text{eq}}(\mathbf{x}, t)$ is commonly chosen as [39]

$$g_{i,k}^{\text{eq}} = C_k[J_i + K_i\mathbf{c}_i \cdot \mathbf{u}] \tag{10}$$

where K_i is constant and equals 1/2 for two-dimensional case. C is the concentration.

For mass transport simulation, the D2Q9 square lattice for 2D simulation can be reduced to D2Q5 square lattice by ignoring velocities at the diagonals, namely four velocities with subscript i greater than 4 in Eq. (2). This reduction of discrete velocities does not create loss of accuracy [39,40].

J_i in Eq. (10) is given by [39]

$$J_i = \begin{cases} J_0, & i = 0 \\ (1 - J_0)/4, & i = 1,2,3,4 \end{cases} \tag{11}$$

where the rest fraction J_0 can be selected from 0 to 1 depending on the diffusivity D. Species concentration C is obtained by

$$C_k = \sum g_{i,k} \tag{12}$$

The diffusivity in lattice unit is related to the collision time by

$$D_k = C_Q(1 - J_0)(\tau_{D,k} - 0.5)\frac{\Delta x^2}{\Delta t} \tag{13}$$

where C_Q is a lattice dependent coefficient and equals 1/2 for 2D simulation [39].

Eqs. (9) and (10) can be recovered to the following advection–diffusion equation for concentration C using Chapman–Enskog expansion

$$\frac{\partial C_k}{\partial t} + \mathbf{u} \cdot \nabla C_k = \nabla \cdot (D_k \nabla C_k) \tag{14}$$

2.1.3. LB model for proton conduction

The macro governing equation of proton conduction is similar to that of mass transport, both of which are passive-scalar transport equations. Thus, similar to that in Section 2.1.2, for proton conduction the evolution of LB equation is as follows

$$h_i(\mathbf{x} + \mathbf{c}_i\Delta t, t + \Delta t) - h_i(\mathbf{x}, t) = -\frac{1}{\tau_h}(h_i(\mathbf{x}, t) - h_i^{\text{eq}}(\mathbf{x}, t)) \tag{15}$$

where h_i is the potential distribution function. Note that the macro velocity $\mathbf{u}$ is zero for proton conduction, thus, the equilibrium concentration distribution function $h_i^{\text{eq}}(\mathbf{x}, t)$ for the D2Q5 lattice is

$$h_i^{\text{eq}} = \begin{cases} K_0\eta, & i = 0 \\ \frac{(1 - K_0)}{4}\eta, & i = 1,2,3,4 \end{cases} \tag{16}$$

where the rest fraction K_0 can also be selected from 0 to 1 depending on the proton conductivity σ. Potential η is obtained by

$$\eta = \sum h_i \tag{17}$$

The proton conductivity in lattice unit is related to the collision time by

$$\sigma = \frac{1}{2}(1 - K_0)(\tau_\sigma - 0.5)\frac{\Delta x^2}{\Delta t} \tag{18}$$

The following conduction equation of proton can be obtained from Eqs. (15) and (16) using Chapman–Enskog expansion method

$$\frac{\partial \eta}{\partial t} = \nabla \cdot (\sigma\nabla\eta) \tag{19}$$

2.2. Brief introduction to FVM

FVM is the most widely adopted numerical method for fluid flow and heat transfer due to its conservation properties of the discretized equation and the clear physical meaning of the coefficients. The differential governing equations are as follows [41]

$$\frac{\partial(\rho\phi)}{\partial t} + \nabla(\rho\mathbf{u}\phi) = \nabla(\Gamma_\phi\nabla\phi) + S_\phi \tag{20}$$

where ϕ is a scalar dependent variable (such as velocity, temperature and concentration). Γ is the nominal diffusion coefficient, and S_ϕ is the source term.

In this article, the two-dimensional IDEAL collocated grid algorithm is adopted [42,43], and the SGSD scheme [44] is used to discretize the convective term.

3. Coupled simulation strategy

3.1. Reconstruction operator

Attention now is turned to design the coupling principle between FVM and LBM. The critical task and major difficulty in the coupled modeling strategy is how to exchange information at the interface of neighboring sub-domains, or essentially between different numerical methods [27,28]. For the coupling between LBM and FVM, it is straightforward to transfer the distributions functions obtained in the LBM framework to macro variables (velocity, density, temperature, concentration and so on) through statistic methods [35]. However, evaluation of the distribution function in LBM from macroscopic variables is not straightforward, since the expansion of a small number of macroscopic variables into a large number of particle distribution functions in LBM is not unique and quite difficult to implement [28]. Thus, operators that reconstruct the distribution function in the LBM from the macro are required, and we call them distribution function reconstruction operator (RO). Our group has developed several RO including that transforming macro density and velocity into density distribution functions [30], that transforming macro temperature into temperature distribution functions [32] and that transforming macro concentration into concentration distribution functions [31].

In the present study, the density and concentration distribution function ROs developed in [29,31] are adopted to calculate the density distribution function f and concentration distribution function g from macro density, velocity and concentration

$$f_i = f_i^{(0)} + \varepsilon f_i^{(1)} + \varepsilon^2 f_i^{(2)} + \cdots$$
$$= f_i^{(eq)}\left[1 - \tau \Delta t U_{i\beta} c_s^{-2}(U_{i\alpha}\partial_{x_\alpha}u_\beta + v\partial_{x_\alpha}^2 u_\beta + v\rho^{-1}S_{\alpha\beta}\partial_{x_\alpha}\rho)\right] \quad (21)$$

$$g_i = g_i^{(0)} + \varepsilon g_i^{(1)} + \varepsilon^2 g_i^{(2)} + \cdots$$
$$= g_i^{(eq)}\left[1 - \tau_g \Delta t C^{-1}(U_{i\alpha}\partial_{x_\alpha}^{(1)}C - D\partial_{x_\alpha}\partial_{x_\alpha}C)\right]$$
$$- 0.5\tau_g \Delta t C c_{i\beta}(U_{i\alpha}\partial_{x_\alpha}^{(1)}u_\beta + v\partial_{x_\alpha}\partial_{x_\alpha}u_\beta + \rho^{-1}vS_{\alpha\beta}\partial_{x_\alpha}\rho)$$
$$+ 0.5\tau_g \Delta t \rho^{-1}Y c_{i\beta}c_s^{-2}\partial_{x\beta}^{(1)}\rho \quad (22)$$

where $U_{i\alpha} = c_{i\alpha} - u_\alpha$, $S_{\alpha\beta} = \partial_{x\beta}u_\alpha + \partial_{x\alpha}u_\beta$. For the readers' convenience, the derivation processes of the two ROs are presented in the Appendix where the explanations of the variables and symbols in Eqs. (21) and (22) also are given.

3.2. General simulation procedure

In this section, the basic idea of coupled simulation strategy by coupling FVM and LBM is introduced. Fig. 1 schematically shows a computational domain decomposed in two regions. FVM and LBM are used to simulate fluid flow and mass transport in the left region and right region, respectively. Line MN is the FVM region boundary located in the LBM sub-region, and AB is the LBM region boundary located in the FVM sub-region. Hence, the sub-region between lines AB and MN is the overlapping region in which both LBM and FVM methods are adopted. This arrangement of the interface is convenient for the information exchange between the two neighboring regions [27]. The multi-scale simulation procedures coupling FVM and LBM are summarized as follows. Step 1, with some assumed initial boundary conditions at the line MN, the FVM simulation in the FVM zone is performed. Step 2, after a temporary solution is obtained, the information at the line AB is transformed into the density-velocity distribution function by Eq. (21) and the concentration distribution function by Eq. (22). Step 3, the LBM simulation is carried out in the LBM zone. Step 4, the temporary solution of LBM at the line MN is transported into the macro variables and the FVM simulation is repeated. Step 5, such computation is repeated until the results in the computational domain reach the convergence standard. The convergence standard in the present study is that the relative error between successive 200 iterated steps is less than 1×10^{-7} for variables related such as velocity, concentration or potential.

Here we want to make some comments on the RO and the overlapping region. First, on the interface boundary for LBM, Eq. (21) (Eq. (22)) is adopted to derive the density (concentration) distribution functions from macro density and velocities (concentration). Note that in Eq. (21) $f = f^{(0)} + f^{(1)} + f^{(2)}$ (here we call it CE-2 scheme, in which distribution function up to second order is contained). We point out that for some relatively simple fluid flows, reduced schemes, namely CE-1 scheme in which $f = f^{(0)} + f^{(1)}$ can also be used. As can be seen from their expressions in Appendix, $f^{(0)}$ only contains the density and velocity, $f^{(1)}$ contains the density gradient and velocity gradient (first order space derivative) and $f^{(2)}$ contains second order space derivative of density and velocity. Thus for fluid flows with second order space derivatives of density and velocity of zero, CE-1 is sufficient. Note that when the first order space derivatives of density and velocity are zero, it means the density and velocities in the whole domain are constant, which do not require numerical simulations. Thus CE-0 scheme where $f = f^{(0)}$ is not used generally. In our simulations, the fluid flow in PEMFC is complex and thus CE-2 is necessary. In fact, even for the relatively simple Poiseuille flow, the second order space derivatives of velocities are not zero.

For deriving concentration distribution functions from concentration, also CE-1 and CE-2 schemes can be used depending on the specific mass transport problems studied. For mass transport problems with constant concentration gradient, CE-1 is sufficient. Albuquerque et al. [45] coupled FDM (finite difference method) and LBM for a two-dimensional (2D) pure diffusion system where the concentration gradient is constant, and in their simulations CE-1 scheme leads to good accuracy. Leemput et al. [46] coupled LBM and FDM for diffusion system with bulk reaction where second order spaced derivatives of concentration are not zero, and thus they used CE-2 scheme. In our simulations for mass transport in PEMFC, CE-2 is required.

The overlapping region is necessary for coupling FVM and LBM in our simulations. This is because for SIMPLE algorithm used in FVM, the boundary nodes are not solved and the values of the physical quantities at the boundary nodes are specified by the users at each time step. Thus, if there is no overlapping region between LBM region and FVM region, the values of the physical quantities at the interface will fix as the initial values specified. Then, another question arises, namely how to determine the size of the overlapping region? It is obvious that information exchange is increasingly sufficient if the size of the overlapping region in-

Fig. 1. Computational domain decomposed into two sub-regions.

creases. However, too large overlapping region is not allowed which is a waste of computational resources. Besides, for using the coupled simulation strategy for fluid flow and mass transport in PEMFC, a coarse (FVM region)–fine (LBM region) grid system is required for saving computation recourses. If the overlapping region is too small, there will be less than a grid in the overlapping region for FVM which certainly causes insufficient information exchange. Thus, in our work, the size of the overlapping region for simulating fluid flow and mass transport in PEMFC is 10 with the lattice space step being of 1, and we can obtain a maximum grid size ratio of 10:1 between FVM region and LBM region.

4. Computational domain and boundary conditions

4.1. Computational domain

The two-dimensional computational domain representing the PEMFC cathode in the along-the-channel direction is shown in Fig. 2, including a rectangle GC, a porous GDL, and a CL with idealized microstructures. The black obstacles in the GDL describe the carbon fibers and the porosity of the GDL is about 0.7.

CL in PEMFC has complex microstructures composed of three phases including carbon, platinum (Pt), ionomer and pores. Carbon allows the conduction of electrons, Pt serves as the catalyst for electrochemical reactions, ionomer provides pathway for proton conduction and void space allows reactant and product gases to diffuse. Indeed, it is a great challenge to reconstruct the realistic porous structures of the CL due to its complex compositions [24]. According to the basic features of the CL, an idealized microstructure of CL with thickness of 20 μm is constructed in this study, as shown in Fig. 2, with periodic repeating units composed of rectangular solid phase and void space (see dashed rectangle in Fig. 2(b) for a typical unit). The solid phase is assumed to be a mixture of electrolyte/electronic phase. Protons migrate into the mixed phase from the PEM (the top bottom of the computational domain) and oxygen diffuses into the void space from the GDL. Electrochemical reaction takes place at the interface (red thin film in Fig. 2(b)) between the solid phase and the void space (The interface is assumed to be completely activated by Pt and thus is completely available for reaction) and the local current density generated by the reaction is determined by the Tafel equation

$$I_{local} = I_{ref} \left(\frac{C_o}{C_{o,ref}} \right)^{r_c} \exp \left(\frac{\alpha F}{RT} \eta \right) \tag{23}$$

Fig. 2. Computational domain representing cathode side of PEMFC, (a) entire computational domain including a GC, a porous GDL and a CL with idealized porous structures and (b) idealized porous structures of CL.

where I_{ref} is the reference exchange current density, α is the transfer coefficient and R is the gas constant. η is the local surface over-potential. r_c is the cathode concentration dependence. $C_{o,ref}$ is the oxygen reference concentration. Note that the idealized CL microstructures is similar to that used in [18]. Also as in [18], electron transport is neglected because proton transport is assumed to be the limiting factor for the oxygen reduction reaction. The proton conductivity in the mixture phase is determined by the following equation [18]

$$\sigma = \sigma_0 \cdot \left(\frac{\varepsilon_e}{1 - \varepsilon_g} \right)^{1.5} \tag{24}$$

where σ_0 is the intrinsic conductivity of the electrolyte, and ε_e and ε_g are the electrolyte and pore volume fractions, respectively.

The computational domain constructed above is divided into two sub-domains: GC, and porous region including GDL and CL. FVM is used to simulate fluid flow and mass transport in GC, while LBM is adopted to simulate fluid flow and mass transport in GDL as well as to simulate fluid flow, mass transport, proton conduction and electrochemical reaction in CL, as shown in Fig. 2(a). Since proton transfer completely takes place in the sub-domain using LBM, coupling between FVM and LBM for proton transfer is not required; only coupling between FVM and LBM for fluid flow and mass transport is implemented at the interfaces of the two sub-domains.

The size of the computational domain is 1000×320 μm, with GC height of 200 μm, GDL height of 100 μm and CL height of 20 μm (The width of each unit in CL is 10 μm). The GC is extended by 300 μm to achieve the fully-developed boundary condition at the GC outlet. Besides, 5 μm is added to the top boundary of the whole domain representing the PEM from where proton transfers into the computational domain. When dividing the whole computational domain into two parts using coupled modeling strategy, the height of the FVM sub-domain is 190 μm, the height of the LBM sub-domain is 145 μm and the width of the overlapping region is 10 μm, as shown in Fig. 2(a). The final size of the computational domain is 1300×325 μm, which is descritized by 1300×325 lattices with a resolution of 1 μm per grid after grid independency check.

It is worth mentioning that in the present work the primary objective is to illustrate the implementation of the coupled simulating strategy. Thus the present study does not completely consider the realistic porous geometries of the GDL and CL in detail; instead it adopts a GDL with simplified porous structures and a CL with idealized microstructures. However, the coupled simulating strategy developed is applicable for real structures of GDL and CL, as there is no essential difference in the schemes of treating obstacles with simplified or realistic structures in the framework of LBM. In fact, coupled simulating strategy proposed in this work can eliminate, to a great extent, the dependence of numerical models on macroscopic geometrical parameters of the porous components (such as porosity and tortuosity) as well as constitutive relations between macroscopic transport properties and the macroscopic structural parameters. This is also one of the major objectives that motivates us to develop the coupled simulating strategy.

4.2. Boundary conditions

The transport processes and the electrochemical reactions in the computational domain can be briefly described as follows: the reactant (air in the present study) is supplied into GC from the GC inlet, penetrates through the porous GDL, and diffuses into the void space in CL; meanwhile, the proton transfers from the top surface of the computational domain (PEM) and conducts through the mixture phase into the CL; at the interface between the void space and mixture phase in the CL, the proton and reactants react,
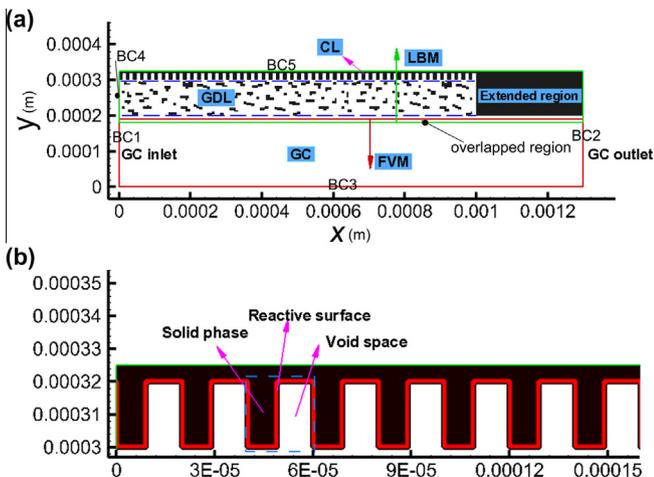
generating current density and water vapor; the water vapor generated then transports through the GDL and is finally removed out of the GC. The boundary conditions for simulating the above processes are presened in the following sections. Section 4.2.1 describes the boundary conditions expressed by macro variables in the whole computational domain and Section 4.2.2. discusses how to implement these boundary conditions involved in the LBM region in the LBM framework.

4.2.1. Boundary conditions for macro variables

At the GC inlet (BC1), uniform air velocity and concentration fraction of species are specified

$$u = u_{in}, \quad v = 0, \quad C_o = 0.21, \quad C_n = 0.79, \quad C_w = 0 \tag{25}$$

where the subscripts o, n and w represent oxygen, nitrogen, and water vapor, respectively. In the simulation, only the transport processes of oxygen and water vapor are simulated. Concentration of the nitrogen can be obtained by subtracting the oxygen concentration and water vapor concentration from the total concentration.

At the GC outlet (BC2), GC is extended 300 μm to obtain fully-developed boundary condition:

$$\frac{\partial u}{\partial x} = 0, \quad \frac{\partial v}{\partial x} = 0, \quad \frac{\partial C_o}{\partial x} = 0, \quad \frac{\partial C_n}{\partial x} = 0, \quad \frac{\partial C_w}{\partial x} = 0 \tag{26}$$

On all the solid walls the no-slip boundary condition is applied. Besides, on all the solid walls except the reactive walls no mass flux and no proton flux boundary condition is used (BC3 (bottom wall of GC), BC4 (left and right walls of GDL), and solid surfaces of carbon fibers in GDL)

$$u = 0, \quad v = 0, \quad \frac{\partial C_o}{\partial n} = 0, \quad \frac{\partial C_n}{\partial n} = 0, \quad \frac{\partial C_w}{\partial n} = 0, \quad \frac{\partial \eta}{\partial n} = 0 \tag{27}$$

On the top surface (PEM, BC5), over-potential is specified:

$$\eta = \eta_{in} \tag{28}$$

At the interface between void space and mixture phase in CL, electrochemical reactions take place and the boundary conditions at the reactive interfaces are

$$D_o \frac{\partial C_o}{\partial n} = -\frac{I_{local}}{4F}, \quad D_w \frac{\partial C_w}{\partial n} = \frac{I_{local}}{2F}, \quad \sigma \frac{\partial \eta}{\partial n} = -I_{local} \tag{29}$$

4.2.2. Boundary conditions of distribution functions in LBM

Now attention is turned to how to implement the above boundary conditions that is involved in the LBM region, because distribution functions rather than macro variables are required on the boundaries in the LBM.

Since part of the GC inlet region (BC1) and GC outlet (BC2) is in the LBM region, as shown in Fig. 2(a), LBM boundary conditions at these boundaries should be specified. For fluid flow, at the GC inlet where the velocity is known, the boundary condition proposed by Zou and He [47] is used, which is based on an idea of bounce-back of non-equilibrium distribution. At the GC outlet, the unknown distribution functions of the boundary nodes are set to be equal to the corresponding distribution functions of the neighboring nodes in the fluid to describe the fully-developed boundary conditions. Besides, on the surface of the solid walls in the LBM region, bounce-back scheme is used to achieve the no-slip boundary conditions.

For mass transport, at the GC inlet where the concentration is known, only one distribution function is unknown for the D2Q5 square lattice, which can be easily determined by subtracting the other four known distribution functions from the concentration specified at the GC inlet. At the GC outlet, method similar to that for fluid flow is employed to obtain the fully-developed boundary conditions. On the surface of solid walls without electrochemical reactions, bounce-back scheme is used to achieve the no-flux

boundary condition; for the proton transfer, such scheme is also adopted on these no-reactive walls.

Emphasis is put on the treatment of the reactive surface in the CL where mass flux and proton flux exist (red thin film at the interface of void space and mixture phase, as shown in Fig. 2(b)). We utilize the boundary condition proposed by Kang et al. [40] to determine unknown part of distribution functions. Fig. 3 is a schematic illustration of reactive surface between void domain and solid domain. For oxygen transport, after each streaming process, the unknown distribution function of the red node R on the reactive surface is $g_{2,o}$, while the other four distribution functions are known. Since $g_{2,o}$ enters the fluid domain, $g_{4,o}$ leaves the fluid domain and $g_{1,o}$, $g_{3,o}$ and $g_{0,o}$ do not affect the fluid domain, the following equation can be obtained [40]

$$g_{2,o} - g_{4,o} = -\frac{D_o}{c} \frac{\partial C_o}{\partial n} \tag{30}$$

For a stationary wall, non-equilibrium portion of the distribution function takes on opposite signs in opposite directions [40], thus

$$g_{2,o} + g_{4,o} = g_{2,o}^{eq} + g_{2,o}^{neq} + g_{4,o}^{eq} + g_{4,o}^{neq} = g_{2,o}^{eq} + g_{4,o}^{eq} \tag{31}$$

Combining Eqs. (10), (23), (29), (30) and (31) leads to the following equations

$$\begin{cases} g_{2,o} + g_{4,o} = \frac{1-J_0}{2} C_o \\ g_{2,o} - g_{4,o} = -\frac{1}{c} \frac{I_{ref}}{4F} \frac{C_o}{C_{o,ref}} \exp\left(\frac{\alpha F}{RT} \eta\right) \end{cases} \tag{32}$$

with two unknown variables $g_{2,o}$ and C_o which can be easily solved.

For water vapor transport, the same method can be adopted to determine the unknown distribution function $g_{2,w}$. For proton conduction, the only unknown distribution function is h_4 as proton transfers inside the mixture phase. Because h_4 enters the mixture phase, h_2 leaves the mixture phase and the remaining three distribution functions do not contribute to the computational domain, thus the following equation is obtained [40]

$$h_4 - h_2 = -\frac{\sigma}{c} \frac{\partial \eta}{\partial n} \tag{33}$$

This equation combined with the following equation

$$h_4 + h_2 = h_4^{eq} + h_2^{eq} \tag{34}$$

and Eqs. (16), (23) and (29) leads to the following equations

$$\begin{cases} h_4 + h_2 = \frac{1-K_0}{2} \eta \\ h_4 - h_2 = -\frac{1}{c} I_{ref} \frac{C_o}{C_{o,ref}} \exp\left(\frac{\alpha F}{RT} \eta\right) \end{cases} \tag{35}$$
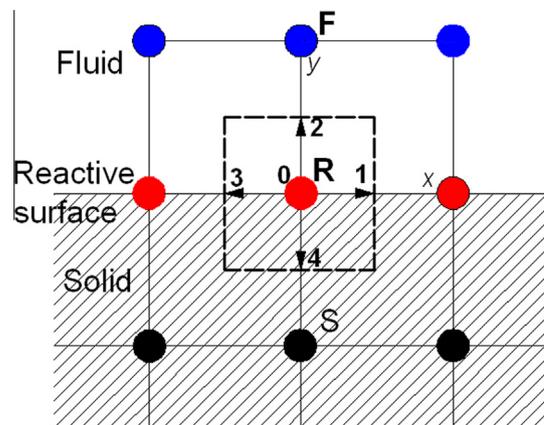
Fig. 3. Schematic of reactive surface.

There are two unknown variables required to be solved, namely h_4 and η. The above equations are nonlinear and Newton–Raphson iteration is used to calculate η. After η is determined, the unknown distribution function h_4 can be easily calculated.

It has been proved by Kang et al. [40] that the above scheme treating the reactive surface guarantees the mass conservation very well. The other reactive surfaces with different normal directions can be treated in the same way as described above.

5. Validation

Several classical flow problems have been used to validate the accuracy and efficiency of the coupled modeling strategy, including flow over a backward-facing step, lid-driven cavity flow, diffusion–convection–reaction problem in a rectangular domain, and natural convection in a square cavity caused by concentration difference. For more details of these validations one can refer to [29,31]. In the present study, single species diffusion in an open rectangular domain [40] is simulated to further validate the coupled modeling strategy. In such a problem, boundary reaction, which is not involved in our previous validations [29,31], is considered. As shown in Fig. 4, species A with constant concentration C_0 diffuses into the rectangular domain with size $a \times b$ and reacts at the top surface with first-order linear kinetics. No-flux boundary condition is used on the bottom boundary and the outlet of the rectangular domain. For such a diffusion and reaction problem, the governing equation and the boundary conditions are

$$\begin{cases} \frac{\partial^2 C_A}{\partial x^2} + \frac{\partial^2 C_A}{\partial y^2} = 0 \\ C_A = C_0, x = 0; \quad D_A \frac{\partial C_A}{\partial y} = -kC_A, \quad y = b \\ \frac{\partial C_A}{\partial y} = 0, \quad y = 0; \quad \frac{\partial C_A}{\partial x} = 0, \quad x = a \end{cases} \tag{36}$$

An analytic solution exists for such problem described by Eq. (36)

$$C_A(x, y) = C_0 \sum_{n=0}^{\infty} \frac{\sin(\beta_n b)}{N_n^2 \beta_n} \frac{\cosh[\beta_n(x - a)]}{\cosh[\beta_n a]} \cos(\beta_n y) \tag{37}$$

where

$$N_n^2 = \frac{b}{2} \left(1 + \frac{\sin(2\beta_n b)}{2\beta_n b}\right) \tag{38-a}$$

$$(\beta_n b) \tan(\beta_n b) = Da = \frac{kb}{D} \tag{38-b}$$
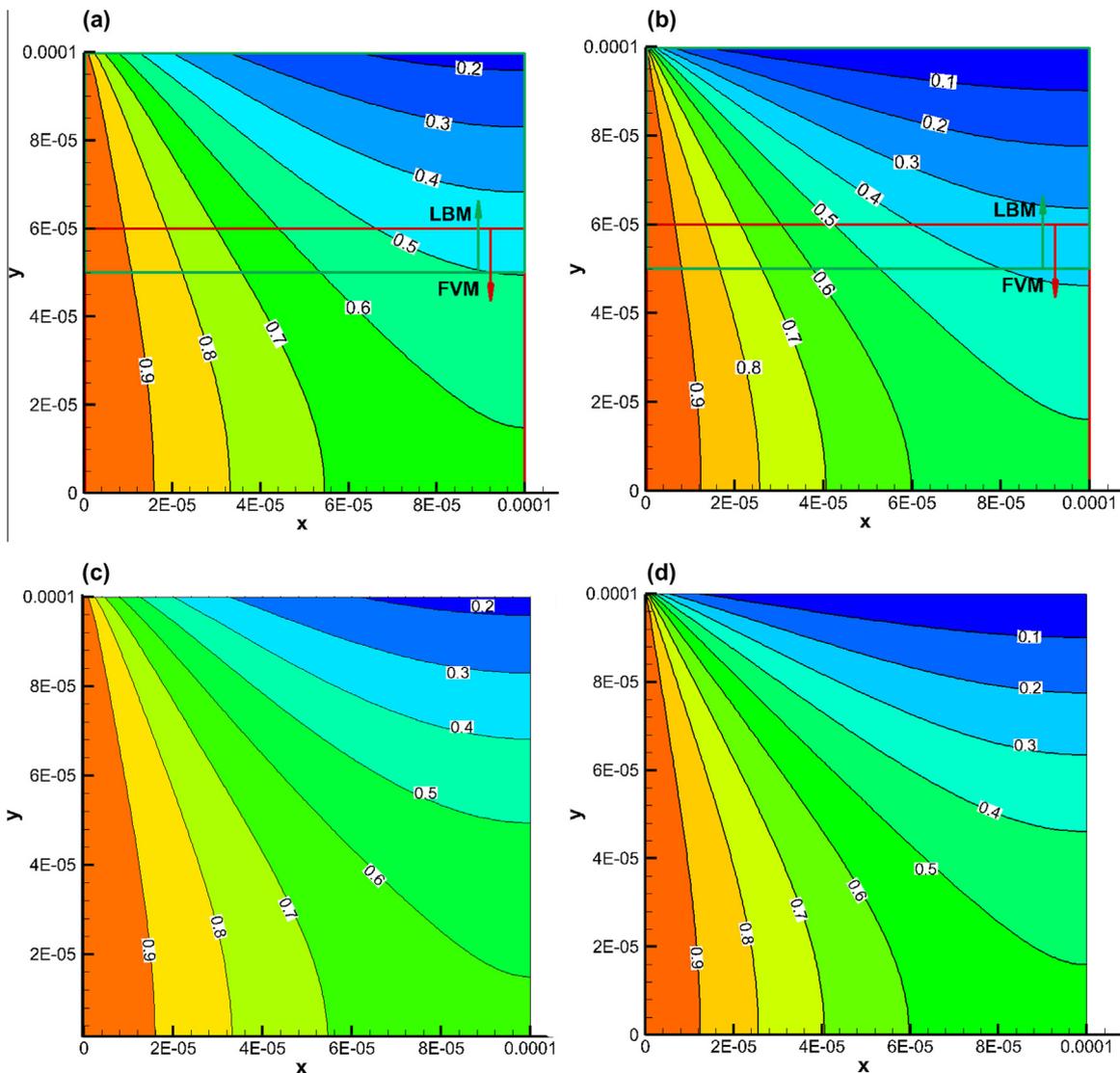
Fig. 4. Comparison of contours of the normalized concentration between simulation results using coupled simulation strategy and analytical solutions for boundary reaction problem, (a) $Da = 5$, coupled simulation strategy, (b) $Da = 50$, coupled simulation strategy, (c) $Da = 5$, analytical solutions and (d) $Da = 50$, analytical solutions.

In Eq. (38-b), _Da_ is a dimensionless number called Damkömohler number, representing the relative strength of reaction to diffusion.

Simulations with large _Da_ of 50 and small _Da_ of 5 are performed using the coupled simulation strategy. In the simulations, $a = 100~\mu m$, $b = 100~\mu m$, $D = 3 \times 10^{-5}~m^2~s^{-1}$. Since in the LBM model, the simulation variables are in the lattice units which should be transformed from corresponding variables in physical units. To connect the lattice space to physical space, length scale l_0, time scale t_0, and density scale ρ_0 are chosen in this study. Accordingly, the physical variables such as velocity u_p, pressure p_p, viscosity v_p and diffusivity D_p can be calculated from the quantities in lattice system (subscripted by L) as follows

$$u_P = u_L \frac{l_0}{t_0}, \quad p_P = p_L \rho_0 \left(\frac{l_0}{t_0}\right)^2, \quad D_P = D_L \frac{l_0^2}{t_0}, \quad v_P = v_L \frac{l_0^2}{t_0} \qquad (39)$$

In the validation as well as other simulations presented in this work, the characteristic parameters are chosen as $l_0 = 1.0 \times 10^{-6}$ m, $t_0 = 1.33 \times 10^{-8}$ s and $\rho_0 = 1.0$ kg m^{-3}.

The domain size is set to 100×100 grids. The lower part of the domain with the size of 100×60 grids is simulated by FVM and the upper part of the domain with the size of 100×50 grids is simulated by LBM, leading to the overlapping region with a size of 100×10. Fig. 4 displays the contours of the normalized concentration C/C_0 obtained from the coupled simulations as well as the analytical solutions, showing an excellent agreement. Careful examinations find that the maximum deviation is less than 0.02%. This provides us strong confidence in further investigation of the multi-scale reactive transport phenomena in PEMFC using the coupled simulation strategy.

6. Results and discussion

In this section, the coupled simulation strategy is used to simulate transport phenomena and electrochemical reactions in the PEMFC cathode. The simulation conditions are listed in Table 1.

6.1. Fluid flow distribution

Fig. 5(a) shows the velocity vector distributions in the computational domain. As expected, there is a large difference in the velocity magnitude between GC and GDL. Due to the blockage of the carbon fibers in GDL, reactant gas mainly flows in the GC and the magnitude of the velocity in GC is significantly greater than that in the GDL, leading to a diffusion-dominated mechanism of mass transport in GDL. Fig. 5(b) displays the local detailed velocity vectors in the blue rectangle in GDL in Fig. 5(a). It can be seen that fluid flow in the GDL is greatly affected by carbon fibers. Our coupled simulation strategy can predict the main flow in the GC as well as capture detailed pore-scale flow within the GDL.

Table 1
Physical parameters.

Quantity	Value
Pressure of the operation condition, P	$1.0 \times 101{,}325$ Pa
Temperature of the operation condition, T	343 K
Universal gas constant, R	8.314 J mol^{-1} K^{-1}
Faraday's constant, F	96,487 C mol^{-1}
Air inlet velocity, u	1.5 m s^{-1}
Diffusivity of oxygen in air, D_O	2.84×10^{-5} m^{2}s^{-1}
Diffusivity of water vapor in air, D_H	3.55×10^{-5} m^2 s^{-1}
Cathode volumetric reference exchange current density/reference oxygen concentration, $A_{cl}j_{ref}/C_{O,ref}$	120 A mol^{-1} (assumed)
Intrinsic conductivity of the electrolyte, σ_0	5 Ω^{-1} m^{-1}
Electrolyte volume fractions, ε_e	0.25
Pore volume fractions, ε_g	0.75
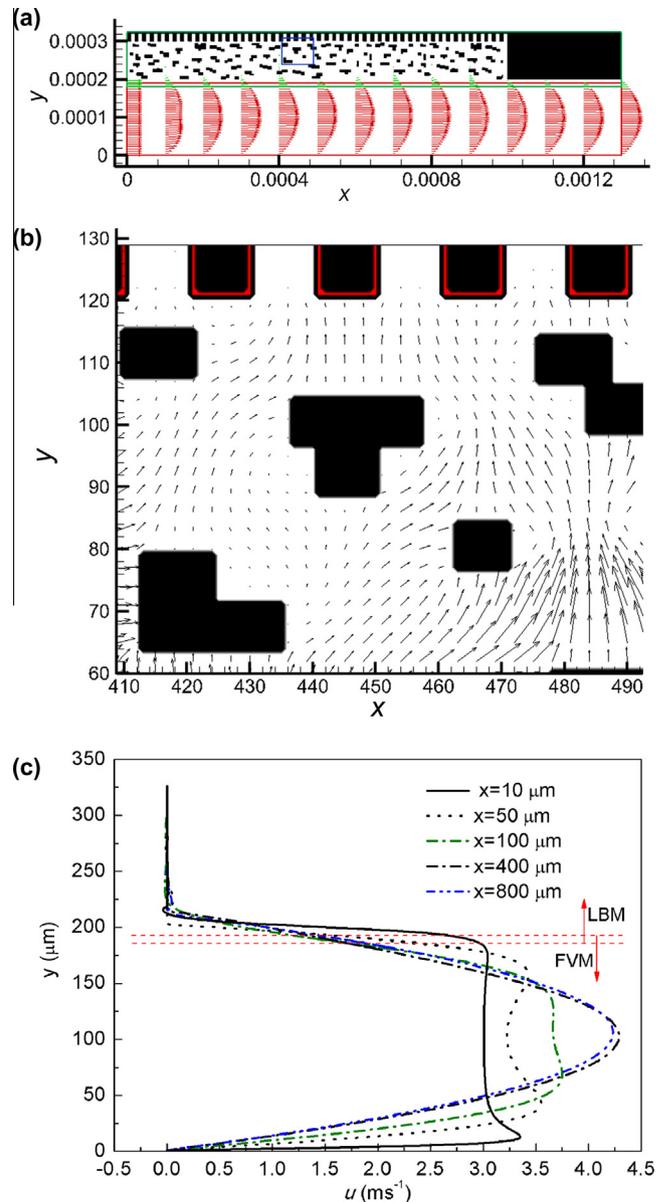
Fig. 5. Velocity distribution, (a) velocity vector distributions in the computational domain, (b) local detailed velocity vectors in the blue rectangle in GDL and (c) x-component velocity u profiles at different cross-sections of the PEMFC cathode side. (For interpretation of the references to color in this figure legend, the reader is referred to the web version of this article.)

The oxygen and water vapor concentration distributions predicted by the coupled simulation strategy are illustrated in Figs. 6 and 7, respectively. Applied over-potential on the top boundary of the computational domain (PEM) is 0.2, 0.6 and 0.8 V, respectively. As can be seen in Fig. 6, oxygen concentration gradually reduces in the flow direction as oxygen is consumed in CL. Besides, oxygen concentration decreases as the over-potential in PEM increases, due to the increased electrochemical reaction rate. In accordance with Fig. 6, water vapor is continuously generated from the electrochemical reaction, resulting in increased water vapor concentration along the channel. In addition, water vapor concentration rises as the over-potential in PEM increases. Note that the mole fraction of oxygen at the reactive sites is about 0.1 in Fig. 6(c), indicating concentration polarization does not occur even the over-potential is as high as 0.8 V. This is due to the relatively short channel used in the present simulation. Besides, it can be seen that
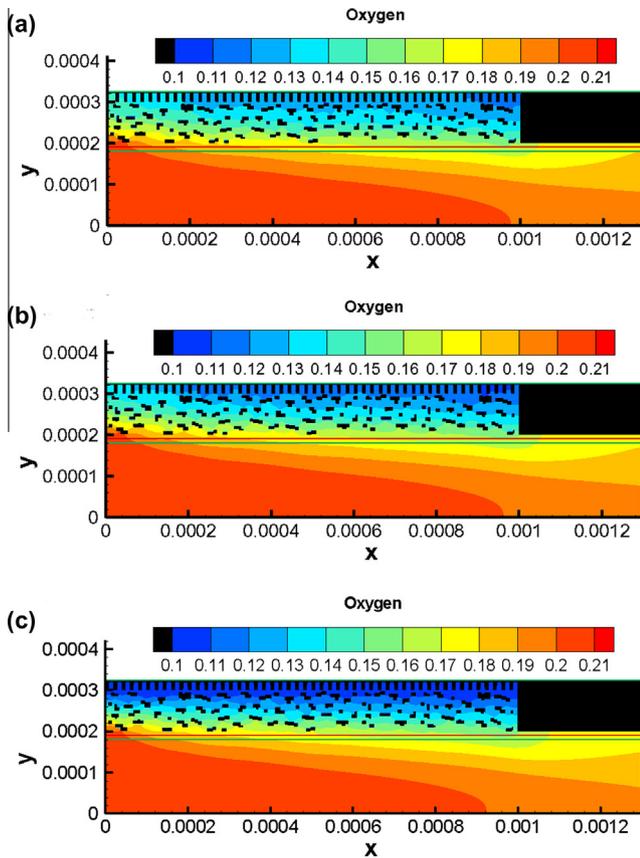
Fig. 6. Oxygen mole fraction distribution under different over-potentials, (a) 0.2 V, (b) 0.6 V and (c) 0.8 V.

Fig. 7. Water vapor mole fraction distribution under different over-potentials, (a) 0.2 V, (b) 0.6 V and (c) 0.8 V.

although a wide range of over-potential is simulated, the difference of mole fraction in the set images of Figs. 6 and 7 is not evident. This is because in our simulations only a small part of the GC near the PEMFC inlet with length of only 1 mm is simulated, which is extremely shorter than the typical length of GCs in PEMFC of a few centimeters. Thus, the concentration difference is not significant.

In fact, fluid flow and mass transport in structures composed by a porous layer and an adjacent clean fluid region, like in GC and GDL considered here, are widely encountered in industrial applications and environment. The key issue related to such transport processes lies in the interface between the clean fluid region and the porous layer, where geometrical properties such as porosity and grain size as well as macroscopic transport properties including permeability and effective diffusivity undergo great changes [48]. Generally, there are two distinct modeling approaches regarding such transport processes: single-domain approach (SDA) and two-domain approach (TDA) [48,49]. The SDA considers the whole composite region as continuum and one set of general governing equations with position-dependent transport properties is applied for the whole domain [49]. Explicit formulation of boundary conditions is avoided at the interface. On the contrary, in the TDA, two sets of governing equations are applied to describe the flow in the clean fluid region (Navier–Stokes equation) and the porous layer (Darcy equation) respectively, and additional boundary conditions are applied at the interface to couple these two sets of equations. Several kinds of interfacial boundary conditions have been proposed in the literature [48]. The accuracy of both SDA and TDA, especially at the interface, depends on the numerical treatment of the interfacial region. In the SDA, the change of the macro transport properties at the interface is achieved by certain artifacts and transport phenomena at the interface depend on the discretization scheme of the governing equations [49]. In the TDA, additional parameters are usually required in the interfacial boundary conditions, which depend on the specific structural characteristics of the porous interface.
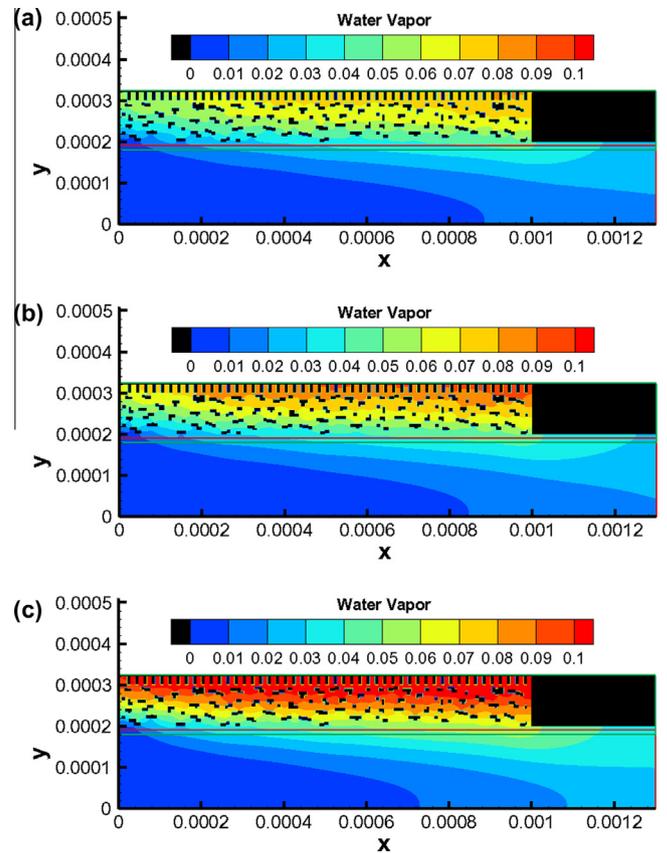
Basically, problems encountered in both SDA and TDA arise from the homogenous treatment of the porous layer in which detailed porous structures of the porous layer are not explicitly considered [31]. Obviously, if real structures of the porous layer are taken into account, the requirement of macro transport properties undergoing large variations at the interface can be released; and thus special treatments of the interfacial region will not be needed [31]. In the present study, the porous structures of the GDL are explicitly considered in the LBM framework and no special treatment is required at the GDL/GC interface. Although large computational resources are required in the LBM compared to homogeneous models used in SDA and TDA, the rapid development of computational techniques increasingly enables the LBM simulations at the pore scale. Fig. 5(c) further shows the x-component velocity u profiles at different cross-sections of the PEMFC cathode side. u uniformly given at the inlet develops into bimodal distributions and then gradually grows into the quasi-parabolic profiles. The local interfacial porous structures of GDL indeed affect the velocity distributions in GC from the comparison of u profiles at x = 400 μm and x = 800 μm.

Commonly, the SDA method is widely used in the modeling and simulation of transport processes in PEMFC. To the best of our knowledge, however, it is found that little attention has been devoted to the interfacial region in the PEMFC, including GDL/GC interface and GDL/CL interface. Actually, interfacial behaviors in PEMFC are of great importance when transport processes in PEMFC

are concerned, especially when two-phase phenomena are considered. Liquid water saturation at the GDL/GC interface greatly affects liquid water content in the GDL [50]. Besides, the capillary pressure required for forming a droplet at the GDL/GC interface plays important roles on liquid water distribution [51] and liquid water dynamic transport processes within the GDL [52]. Therefore, further work is required to investigate the interfacial phenomena in PEMFC where realistic porous structures of GDL are considered, which is ongoing in our group.

6.2. Over-potential distributions

Fig. 8 shows the over-potential distributions in the CL corresponding to Figs. 6 and 7. It can be seen that the potential drop increases as the over-potential in the PEM increases. This is expected because reaction rate increases as over-potential in the PEM increases, leading to more current density generated and thus bigger ohmic loss. In the present study, the CL adopted has an idealized structure with several assumptions, which extremely simplifies the realistic porous complex structures of the CL. It is expected that when the complex multiple phases in CL are considered, more important pore-scale reactive transport phenomena can be observed [19]. Our further work is to use the coupled simulation strategy to study the transport phenomena and electrochemical reactions in PEMFC by taking into account the realistic micro structures of GDL and CL.

6.3. Computational resource saving techniques

In the LBM region, the gird size should be fine enough to resolve the microstructures of the porous components. In the FVM clean region, however, such a fine grid size is not necessary because relatively coarse grid size is enough to capture the transport phenomena in the FVM region. Using the same grid size in the FVM as that in the LBM takes up too many computational resources which can be saved by using different grid sizes in different sub-regions. In

this section, we increase the grid size in the FVM region while fixing the grid size in the LBM region. The grid size ratio between the FVM and LBM ranges is set as 10, 5, 2, and 1 respectively. Fig. 9 schematically shows the interface region between the FVM and LBM using coarse and fine grids with grid ratio of 5:1. Note that in each iteration step of the simulation, the field values at the white open circles on the LBM region interface boundary (fine region boundary AB in Fig. 9) should be interpolated from the results of the neighboring coarse grids. Simply linear interpolation is used in this study to determine the values at the white circles. Besides, the field values at the blue solid circles on the FVM region interface boundary (coarse region boundary MN in Fig. 9) are an averaged value of the neighboring fine grids. The boundary conditions for the simulations with coarse (FVM) – fine (LBM) grid system are the same as that in Section 6.1.

Figs. 10 and 11 show the u and v velocity on the interface boundary of LBM region and FVM region respectively. It can be seen that even for the case with grid ratio 10:1, the simulation results are still in good agreement with that of 1:1 case (Here we assume the result of 1:1 case is the benchmark solution). The u velocities for all the cases are almost coincident except at the region with fluctuations. This is because average (at the FVM interface) and interpolation (at the LBM interface) at regions with large fluctuations obviously lead to large errors, thus the discrepancy increases as the grid ratio increases at these fluctuating regions. The v velocities show some discrepancy, but the overall fluctuation trends for all the cases are consistent. It can be seen that the fluctuations of v velocities on the interface boundary for LBM decrease as the grid ratio increases, while that on the interface boundary of FVM increase as the grid ratio increases. This is because on the interface boundary of LBM the interpolations smooth the fluctuations. On the boundary interface of FVM, the grid of LBM region closest to the FVM grid currently calculated is given the largest weight factor for average, thus somewhat magnifying the fluctuations. Fig. 12 shows the mole fraction of oxygen and water vapor on the interface boundary of LBM with over-potential of 0.5 V. Again the simulation results for all the cases show a good agreement.
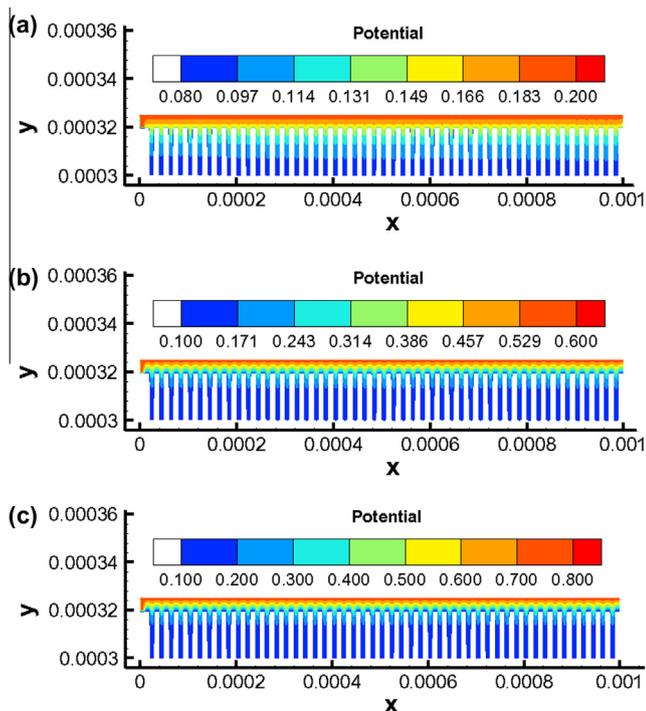
Fig. 8. Potential distributions under different over-potential distributions , (a) 0.2 V, (b) 0.6 V and (c) 0.8 V.
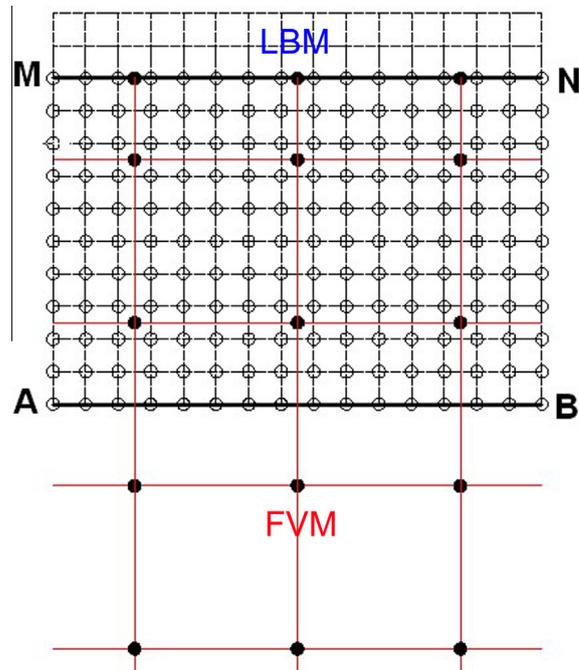
Fig. 9. Interface between FVM region and LBM region using coarse grid and fine grid.
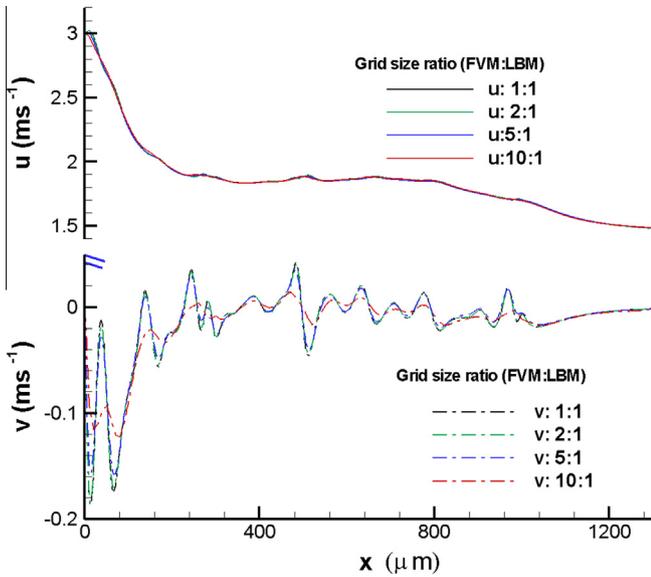
Fig. 10. Velocity on the interface boundary of LBM region with different ratio of grid size between FVM region and LBM region.

Fig. 11. Velocity on the interface boundary of FVM region with different ratio of grid size between FVM region and LBM region.

The maximum grid size ratio between FVM and LBM regions that can guarantee the accuracy depends on several factors. On the one hand, since the width of overlapping region is fixed (10 lattices this study), the maximum ratio is limited (10 in this study) because further increasing the ratio (beyond 10 in this study) leads to less than a FVM grid in the overlapping region which would cause insufficient information exchange. On the other hand, the maximum ratio also depends on the interface position, the local field gradient near the interface, and the algorithms of FVM and LBM. If the interface position is suitably chosen that the local gradient of variables is small, then the maximum ratio of grid size can be increased. Adopting stable and robust algorithms of FVM and LBM can also lead to high maximum grid size ratio.

There are other techniques to save computational resources in the framework of the coupled simulation strategy. A buffer zone can be added between the FVM region and LBM region, which serves as a bridge between the coarse FVM grid and fine LBM grid

Fig. 12. Mole fraction on the interface boundary of FVM region with different ratio of grid size between FVM region and LBM region.

[30], as shown in Fig. 13. The grid size of the buffer zone can be chosen between the FVM grid size and LBM grid size. For example, the grid size of the buffer zone can be set as 4 assuming the grid size of LBM is 1. If the ratio of grid size between FVM region and the buffer region is 4, then the maximum grid size ratio between FVM region and the LBM region can be as big as 16, leading to greatly reduced computational resources. The buffer region can be either solved using FVM or LBM. In addition, multi-block techniques can be used to increase the efficiency of coupled simulation strategy. For example, fine LBM grid can be used to simulate transport phenomena in CL with more compact porous structures and coarse LBM grid can be used to simulate transport phenomena in GDL with relatively larger pores, as shown in Fig. 13. On the whole, a multi-grid system, for example from the coarsest FVM grid in the clean region (GC), to relatively coarse grid in the buffer zone, to relatively fine LBM grid in porous region with large pores (GDL) and finally finest LBM grid in porous media with compact microstructures (CL), as shown in Fig. 13, can be adopted to improve the efficiency of the coupled simulation strategy.

We have to admit that the LBM region takes a majority of the total computational resources required in the coupled simulation strategy, which cannot be easily reduced because realistic micro-
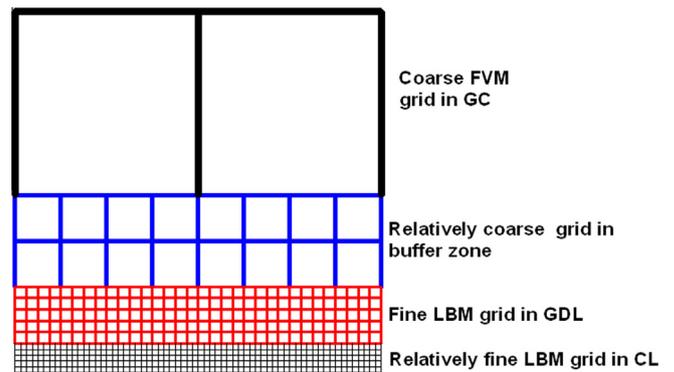
Fig. 13. Schematic of multi grid system adopted in the coupling simulation strategy.

structures of porous components needs to be resolved, although multi-block LBM is of some help. Improving computational efficiency in the LBM region depends on the development of computer simulation capacities.

7. Conclusion

A coupled simulation strategy is used to simulate the multi-scale transport phenomena in PEMFC. In this strategy, different numerical methods are used to predict transport processes in different local regions with different length-scales. Information is exchanged at the interfaces between neighboring regions. During the implementation of coupled modeling strategy, the computational domain is divided into several sub-domains and in each sub-domain the appropriate numerical method corresponding to the length scale of this sub-domain is applied.

In this study, single-phase fluid flow, oxygen and water vapor transport, proton conduction and electrochemical reaction in the cathode side of a PEMFC are simulated using the coupled simulation strategy. During the implementation of the coupled simulation strategy, PEMFC cathode side is divided into two sub-domains, one is GC and the other includes the GDL and CL. Top-down numerical method FVM is used for fluid flow and mass transport in GC sub-domain, while bottom-up numerical method LBM is employed for pore-scale flow and mass transport in GDL and CL and proton conduction in CL. Two ROs transferring macro density and concentration in FVM to density distribution function and concentration distribution function in LBM are used to transfer information at the interface between the two sub-domains. The simulation results show that the coupled simulation strategy is able to capture the pore-scale transport process and electrochemical reactions in porous components of PEMFC.

Computational resource saving techniques in the framework of coupled simulation strategy are also discussed. Coarse grid is used in the FVM region and fine grid is used in LBM region. Good simulation results can be obtained even the ratio of grid size between FVM region and LBM region is 5. Further increasing the grid size ratio to 10 leads to no-ideal results although the simulation is converged. Factors affecting the maximum grid size ratio are discussed, including the interface position, the local variable gradient near the interface and the algorithms of FVM and LBM. A multi-grid system is proposed to simulate transport processes and electrochemical reactions in PEMFC, which consists of coarsest FVM grid in GC, relatively coarse grid in buffer zone, relatively fine LBM grid in GDL, and finally finest LBM grid in CL.

Extending the coupled simulation strategy to the whole PEMFC based on three-dimensional realistic microstructures of GDL and CL is under way, where multi-grid system is adopted.

Acknowledgments

Appendix A

A.1. Reconstruction operator for density distribution function

According to the Chapman–Enskog method, we can introduce the following time and space scale expanding

$$\partial_t = \varepsilon \partial_t^{(1)} + \varepsilon^2 \partial_t^{(2)} \tag{A-1a}$$

$$\partial_{x_\alpha} = \varepsilon \partial_{x_\alpha}^{(1)} \tag{A-1b}$$

the small expansion parameter ε can be viewed as the Knudsen number Kn which is the ratio of the mean free path over the characteristic length scale of the flow, and α represents the two coordinate directions.

The distribution function f_i is expanded around the distributions $f_i^{(0)}$ as follows

$$f_i = f_i^{(0)} + \varepsilon f_i^{(1)} + \varepsilon^2 f_i^{(2)} \tag{A-2}$$

With

$$\sum_i f_i^{(1)} = 0, \quad \sum_i \mathbf{c}_i f_i^{(1)} = 0, \quad \sum_i f_i^{(2)} = 0, \quad \sum_i \mathbf{c}_i f_i^{(2)} = 0 \tag{A-3}$$

Then, $f_i(\mathbf{x} + \mathbf{c}_i \Delta t, t + \Delta t)$ in Eq. (1) is expanded about x and t which gives

$$f_i(\mathbf{x} + \mathbf{c}_i \Delta t, t + \Delta t) = f_i(\mathbf{x}, t) + \Delta t D_{i\alpha} f_i(\mathbf{x}, t) + \frac{(\Delta t)^2}{2} D_{i\alpha}^2 f_i(\mathbf{x}, t) + O[(\Delta t)^3] \tag{A-4}$$

where $D_{i\alpha} = \partial_t + c_i \partial_{x_\alpha}$ for concise expression.

Substituting Eq. (A-4) into Eq. (1) yields the following equation

$$\Delta t D_{i\alpha} f_i + \frac{(\Delta t)^2}{2} D_{i\alpha}^2 f_i = -\frac{1}{\tau_f} (f_i - f_i^{(eq)}) + O[(\Delta t)^3] \tag{A-5}$$

Furthermore, substituting Eqs. (A-1) and (A-2) into Eq. (A-5) obtains

$$\varepsilon D_{i\alpha}^{(1)} f^{(0)} + \varepsilon^2 \left[D_{i\alpha}^{(1)} f_i^{(1)} + \partial_t^{(2)} f_i^{(0)} \right] + \varepsilon^2 \frac{\Delta t}{2} \left[D_{i\alpha}^{(1)} \right]^2 f_i^{(0)}$$
$$= -\frac{1}{\Delta t \tau_f} \left(f_i^{(0)} + \varepsilon f_i^{(1)} + \varepsilon^2 f_i^{(2)} - f_i^{(eq)} \right) + O[(\Delta t)^3] \tag{A-6}$$

Then by matching the scales of ε^0, ε^1 and ε^2, we have

$$\varepsilon^0: \quad f_i^{(0)} = f_i^{eq} \tag{A-7}$$

$$\varepsilon^1: \quad f_i^{(1)} = -\Delta t \tau_f D_{i\alpha}^{(1)} f_i^{(0)} + O[(\Delta t)^2] \tag{A-8}$$

$$\varepsilon^2: \quad f_i^{(2)} = -\Delta t \tau_f \left[D_{i\alpha}^{(1)} f_i^{(1)} + \partial_t^{(2)} f_i^{(0)} \right] - \tau_f \frac{(\Delta t)^2}{2} \left[D_{i\alpha}^{(1)} \right]^2 f_i^{(0)} + O[(\Delta t)^3] \tag{A-9}$$

Considering Eqs. (4) and (5), we can sum Eq. (A-8) over the phase space. Then the first order of the continuity equation and momentum equation can be derived

$$\varepsilon^1: \quad \partial_t^{(1)} \rho + \partial_{x_\alpha}^{(1)} (\rho u_\alpha) + O[(\Delta t)^2] = 0 \tag{A-10}$$

$$\partial_t^{(1)} (\rho u_\alpha) + \partial_{x_\beta}^{(1)} (\rho u_\alpha u_\beta + p\delta_{\alpha\beta}) + O[(\Delta t)^2] = 0 \tag{A-11}$$

By the same way, we can obtain the second order of continuity equation and momentum equation according to Eq. (A-9)

$$\varepsilon^2: \quad \partial_t^{(2)} \rho + O[(\Delta t)^3] = 0 \tag{A12-a}$$

$$\partial_t^{(2)} (\rho u_\alpha) - \nu \partial_{x_\beta}^{(1)} \left\{ \rho \left[\partial_{x_\alpha}^{(1)} u_\beta + \partial_{x_\beta}^{(1)} u_\alpha \right] \right\} + O[(\Delta t)^3] = 0 \tag{A12-b}$$

The formulas according to the chain rule of derivatives read:

$$\partial_t f_i^{eq} = \partial_\rho f_i^{eq} \partial_t \rho + \partial_{u_\beta} f_i^{eq} \partial_t u_\beta \tag{A-13a}$$

$$\partial_{x_\alpha} f_i^{eq} = \partial_\rho f_i^{eq} \partial_{x_\alpha} \rho + \partial_{u_\beta} f_i^{eq} \partial_{x_\alpha} u_\beta \tag{A-13b}$$

From Eq. (3), we can get

$$\partial_{u_\beta} f_i^{eq} = \omega_i \rho \left[\frac{1}{c_s^2} (c_{i\beta} - u_\beta) + \frac{1}{c_s^4} c_{i\alpha} c_{i\beta} u_\alpha \right] \tag{A-14a}$$

$$\partial_\rho f_i^{eq} = \frac{1}{\rho} f_i^{eq} \tag{A-14b}$$

Furthermore, substituting Eqs. (A-10)-(A.14) into Eq. (A-8), we can derive the first order expression of distribution function f_i

$$f_i^{(1)} = -\tau_f \Delta t \left[\partial_t^{(1)} f_i^{(0)} + \mathbf{c}_i \partial_{x_\alpha}^{(1)} f_i^{(0)} \right]$$

$$= -\tau_f \Delta t \left[\partial_\rho f_i^{(0)} \partial_t^{(1)} \rho + \partial_{u_\beta} f_i^{(0)} \partial_t^{(1)} u_\beta + \mathbf{c}_i \left(\partial_\rho f_i^{(0)} \partial_{x_\alpha}^{(1)} \rho + \partial_{u_\beta} f_i^{(0)} \partial_{x_\alpha}^{(1)} u_\beta \right) \right]$$

$$= -\tau_f \Delta t \left[U_{i\alpha} f_i^{(0)} \frac{1}{\rho} \partial_{x_\alpha}^{(1)} \rho + U_{i\alpha} \omega_i \rho \left(\frac{1}{c_s^2} U_{i\beta} + \frac{1}{c_s^4} c_{i\beta} c_{i\gamma} u_\gamma \right) \partial_{x_\alpha}^{(1)} u_\beta \right.$$

$$\left. - f_i^{(0)} \partial_{x_\alpha}^{(1)} u_\alpha - \omega_i \left(\frac{1}{c_s^2} U_{i\alpha} + \frac{1}{c_s^4} c_{i\alpha} c_{i\gamma} u_\gamma \right) \partial_{x_\alpha}^{(1)} p \right] \tag{A-15}$$

where $U_{i\alpha} = c_{i\alpha} - u_\alpha$.

The second-order expression of f_i in Eq. (A-9) is calculated as follows

$$f_i^{(2)} = -\Delta t \tau_f \left[D_{i\alpha}^{(1)} f_i^{(1)} + \partial_t^{(2)} f_i^{(0)} \right] - \frac{(\Delta t)^2 \tau_f}{2} \left[D_{i\alpha}^{(1)} \right]^2 f_i^{(0)}$$

$$= -\Delta t \tau_f \left[D_{i\alpha}^{(1)} \left(-\tau \Delta t D_{i\alpha}^{(1)} f_i^{(0)} \right) + \partial_t^{(2)} f_i^{(0)} \right]$$

$$- \frac{(\Delta t)^2 \tau_f}{2} \left[D_{i\alpha}^{(1)} \right]^2 f_i^{(0)}$$

$$= -\Delta t \tau_f \partial_t^{(2)} f_i^{(0)} + (\Delta t)^2 \tau_f \left(\tau_f - \frac{1}{2} \right) \left[D_{i\alpha}^{(1)} \right]^2 f_i^{(0)} \tag{A-16}$$

We can ignore the second-order derivative of $f_i^{(2)}$, then

$$f_i^{(2)} = -\Delta t \tau_f \partial_t^{(2)} f_i^{(0)} \tag{A-17}$$

By the chain rule of derivatives, it gives

$$\partial_t^{(2)} f_i^{(0)} = \partial_\rho f_i^{(0)} \partial_t^{(2)} \rho + \partial_{u_\beta} f_i^{(0)} \partial_t^{(2)} u_\beta = \partial_{u_\beta} f_i^{(0)} \partial_t^{(2)} u_\beta \tag{A-18}$$

Using Eqs. (A-12b) and (A-14), we get

$$\partial_t^{(2)} f_i^{(0)} = \partial_{u_\beta} f_i^{(0)} \partial_t^{(2)} u_\beta = \frac{1}{\rho} \partial_{u_\beta} f_i^{(0)} \partial_t^{(2)} (\rho u_\beta)$$

$$= v \omega_i \left[\frac{1}{c_s^2} (c_{i\beta} - u_\beta) + \frac{1}{c_s^4} c_{i\alpha} c_{i\beta} u_\alpha \right] \partial_{x_\alpha}^{(1)} \left(\rho \left(\partial_{x_\alpha}^{(1)} u_\beta + \partial_{x_\beta}^{(1)} u_\alpha \right) \right)$$

$$= v \omega_i \rho \left[\frac{1}{c_s^2} (c_{i\beta} - u_\beta) + \frac{1}{c_s^4} c_{i\alpha} c_{i\beta} u_\alpha \right]$$

$$\times \left[\frac{1}{\rho} \partial_{x_\alpha}^{(1)} \rho \left(\partial_{x_\alpha}^{(1)} u_\beta + \partial_{x_\beta}^{(1)} u_\alpha \right) + \partial_{x_\alpha}^{(1)} \left(\partial_{x_\alpha}^{(1)} u_\beta + \partial_{x_\beta}^{(1)} u_\alpha \right) \right] \tag{A-19}$$

So the following expression is obtained

$$f_i^{(2)} = -\Delta t \tau_f v \omega_i \rho \left(\frac{1}{c_s^2} U_{i\beta} + \frac{1}{c_s^4} c_{i\alpha} c_{i\beta} u_\alpha \right)$$

$$\times \left[\frac{1}{\rho} \partial_{x_\alpha}^{(1)} \rho \left(\partial_{x_\alpha}^{(1)} u_\beta + \partial_{x_\beta}^{(1)} u_\alpha \right) + \partial_{x_\alpha}^{(1)} \left(\left(\partial_{x_\alpha}^{(1)} u_\beta + \partial_{x_\beta}^{(1)} u_\alpha \right) \right) \right] \tag{A-20}$$

Here, we introduce an approximation of $\partial_{u_\beta} f_i^{(0)}$ by dropping terms of a higher order than u^2 as follows

$$\partial_{u_\beta} f_i^{(0)} = \omega_i \rho \left(\frac{1}{c_s^2} U_{i\beta} + \frac{1}{c_s^4} c_{i\beta} c_{i\gamma} u_\gamma \right) \approx \frac{U_{i\beta}}{c_s^2} f_i^{(0)} \tag{A-21}$$

Assuming the velocity fields is divergence-free, written as

$$\partial_{x_\alpha} u_\alpha = 0 \tag{A-22}$$

According to Eqs. (A-21) and (A-22), we can rewrite the expressions of $f_i^{(1)}$ and $f_i^{(2)}$ as

$$f_i^{(1)} = -\tau_f \Delta t \left[U_{i\alpha} f_i^{(0)} \frac{1}{\rho} \partial_{x_\alpha}^{(1)} \rho + U_{i\alpha} U_{i\beta} f_i^{(0)} \frac{1}{c_s^2} \partial_{x_\alpha}^{(1)} u_\beta - U_{i\alpha} f_i^{(0)} \frac{1}{\rho c_s^2} \partial_{x_\alpha}^{(1)} p \right]$$

$$= -\tau_f \Delta t U_{i\alpha} U_{i\beta} f_i^{(0)} c_s^{-2} \partial_{x_\alpha}^{(1)} u_\beta \tag{A-23}$$

$$f_i^{(2)} = -\Delta t \tau_f v U_{i\beta} f_i^{(0)} c_s^{-2} \left[\frac{1}{\rho} \partial_{x_\alpha}^{(1)} \rho \left(\partial_{x_\alpha}^{(1)} u_\beta + \partial_{x_\beta}^{(1)} u_\alpha \right) + \left(\partial_{x_\alpha}^{(1)} \right)^2 u_\beta \right]$$

$$= -\Delta t \tau_f v U_{i\beta} f_i^{(0)} c_s^{-2} \left[\frac{1}{\rho} S_{\alpha\beta}^{(1)} \partial_{x_\alpha}^{(1)} \rho + \left(\partial_{x_\alpha}^{(1)} \right)^2 u_\beta \right] \tag{A-24}$$

where $S_{\alpha\beta} = \partial_{x_\beta} u_\alpha + \partial_{x_\alpha} u_\beta$.

Finally, we can derive the expression of f_i

$$f_i = f_i^{(0)} + \varepsilon f_i^{(1)} + \varepsilon^2 f_i^{(2)}$$

$$= f_i^{(0)} - \tau \Delta t U_{i\alpha} U_{i\beta} f_i^{(0)} c_s^{-2} \partial_{x_\alpha} u_\beta$$

$$- \tau \Delta t v U_{i\beta} f_i^{(0)} c_s^{-2} \left[\frac{1}{\rho} S_{\alpha\beta} \partial_{x_\alpha} \rho + \partial_{x_\alpha}^2 u_\beta \right]$$

$$= f_i^{(eq)} \left[1 - \tau \Delta t U_{i\beta} c_s^{-2} \left(U_{i\alpha} \partial_{x_\alpha} u_\beta + v \partial_{x_\alpha}^2 u_\beta + v \rho^{-1} S_{\alpha\beta} \partial_{x_\alpha} \rho \right) \right] \tag{A-25}$$

Eq. (A-25) is an analytic expression for reconstructing the density distribution function from the macro variables. We call it as density distribution function reconstruction operator.

Appendix B. Reconstruction operator for concentration distribution function

Following Eqs. (A-2)–(A-9), we can obtain g_i in the scales of ε^0, ε^1 and ε^2

$$\varepsilon^0: \quad g_i^{(0)} = g_i^{eq} \tag{B-1}$$

$$\varepsilon^1: \quad g_i^{(1)} = -\Delta t \tau_g D_{i\alpha}^{(1)} g_i^{(0)} + O[(\Delta t)^2] \tag{B-2}$$

$$\varepsilon^2: \quad g_i^{(2)} = -\Delta t \tau_g \left[D_{i\alpha}^{(1)} g_i^{(1)} + \partial_t^{(2)} g_i^{(0)} \right] - \frac{(\Delta t)^2 \tau_g}{2} \left[D_{i\alpha}^{(1)} \right]^2 g_i^{(0)}$$

$$+ O[(\Delta t)^3] \tag{B-3}$$

Therefore, we can derive the macroscopic equations at the $t_1 = \varepsilon t$ and $t_2 = \varepsilon^2 t$ time scales

$$\partial_t^{(1)} C + \partial_{x_\alpha}^{(1)} (u_\alpha C) = 0 \tag{B-4}$$

$$\partial_t^{(2)} C - 2J(\tau - 0.5) \frac{\Delta x^2}{\Delta t} \partial_{x_\alpha}^{(1)} \partial_{x_\alpha}^{(1)} (C) = 0 \tag{B-5}$$

Introducing the formulas according to the chain rule of derivatives

$$\partial_t g_i^{eq} = \partial_Y g_i^{eq} \partial_t C + \partial_{u_\beta} g_i^{eq} \partial_t u_\beta \tag{B-6}$$

$$\partial_{x_\alpha} g_i^{eq} = \partial_Y g_i^{eq} \partial_{x_\alpha} C + \partial_{u_\beta} g_i^{eq} \partial_{x_\alpha} u_\beta \tag{B-7}$$

and from the equilibrium distribution function given by Eq. (10), we can get the following expression

$$\partial_{u_\beta} g_i^{eq} = \partial_{u_\beta} [C(J + 1/2 c_{i\gamma} u_\gamma)] = 1/2 C c_{i\beta} \tag{B-8}$$

$$\partial_Y g_i^{eq} = \partial_Y [C(1 + 1/2 c_{i\gamma} u_\gamma)] = C^{-1} g_i^{(eq)} \tag{B-9}$$

The first order expression of distribution function g_i can be derived as

$$g_i^{(1)} = -\tau_g \Delta t D_i^{(1)} g_i^{(0)} = -\tau_g \Delta t \left(\partial_t^{(1)} g_i^{(0)} + c_{i\alpha} \partial_{x_\alpha}^{(1)} g_i^{(0)} \right)$$

$$= -\tau_g \Delta t \left[\partial_Y g_i^{(0)} \partial_t^{(1)} C + \partial_{u_\beta} g_i^{(0)} \partial_t^{(1)} u_\beta + c_{i\alpha} \left(\partial_Y g_i^{(0)} \partial_{x_\alpha}^{(1)} C + \partial_{u_\beta} g_i^{(0)} \partial_{x_\alpha}^{(1)} u_\beta \right) \right]$$

$$= -\tau_g \Delta t \left[-\partial_Y g_i^{(0)} \partial_{x_\alpha}^{(1)} (u_\alpha C) - u_\alpha \partial_{u_\beta} g_i^{(0)} \partial_{x_\alpha}^{(1)} u_\beta \right.$$

$$\left. - \frac{1}{\rho} \partial_{u_\beta} g_i^{(0)} \partial_{x_\beta}^{(1)} p + c_{i\alpha} \left(\partial_Y g_i^{(0)} \partial_{x_\alpha}^{(1)} C + \partial_{u_\beta} g_i^{(0)} \partial_{x_\alpha}^{(1)} u_\beta \right) \right]$$

$$= -\tau_g \Delta t \left[U_{i\alpha} C^{-1} g_i^{(eq)} \partial_{x_\alpha}^{(1)} C + 0.5 U_{i\alpha} C c_{i\beta} \partial_{x_\alpha}^{(1)} u_\beta - 0.5 \rho^{-1} C c_{i\beta} \partial_{x_\beta}^{(1)} p \right] \tag{B-10}$$

The second order expression of distribution function g_i can be derived as

$$g_i^{(2)} = -\tau_g \Delta t \left\{ \partial_t^{(2)} g_i^{(0)} + \left(1 - \frac{1}{2\tau_g}\right) D_i^{(1)} g_i^{(1)} \right\}$$

$$= -\tau_g \Delta t \left\{ \partial_t^{(2)} g_i^{(0)} - \left(\tau_g - \frac{1}{2}\right) \Delta t D_i^{(1)} \left[D_i^{(1)} g_i^{(0)} \right] \right\}$$

$$= -\tau_g \Delta t \left[\partial_t^{(2)} g_i^{(0)} - \left(\tau_g - \frac{1}{2}\right) \Delta t \left(D_i^{(1)}\right)^2 g_i^{(0)} \right] \quad \text{(B-11)}$$

The second-order derivative of $g_i^{(0)}$ can be ignored in the above equation, then

$$g_i^{(2)} = -\tau_g \Delta t \partial_t^{(2)} g_i^{(0)} = -\tau_g \Delta t \left[\partial_Y g_i^{(0)} \partial_t^{(2)} C + \partial_{u_\beta} g_i^{(0)} \partial_t^{(2)} u_\beta \right]$$

$$= -\tau_g \Delta t \left[DY^{-1} g_i^{(eq)} \partial_{x_\alpha}^{(1)} \partial_{x_\alpha}^{(1)} C + 0.5 C c_{i\beta} \rho^{-1} \partial_{t_2}(\rho u_\beta) \right]$$

$$= -\tau_g \Delta t \left[DC^{-1} g_i^{(eq)} \partial_{x_\alpha}^{(1)} \partial_{x_\alpha}^{(1)} C + 0.5 C c_{i\beta} \rho^{-1} v \right.$$

$$\left. \times \left[\rho \partial_{x_\alpha}^{(1)} \left(\left(\partial_{x_\alpha}^{(1)} u_\beta + \partial_{x_\beta}^{(1)} u_\alpha\right)\right) + \left(\partial_{x_\alpha}^{(1)} u_\beta + \partial_{x_\beta}^{(1)} u_\alpha\right) \partial_{x_\alpha}^{(1)} \rho \right] \right]$$

$$= -\tau_g \Delta t \left[DC^{-1} g_i^{(eq)} \partial_{x_\alpha}^{(1)} \partial_{x_\alpha}^{(1)} C + 0.5 C c_{i\beta} \rho^{-1} v \left[\rho \partial_{x_\alpha}^{(1)} \partial_{x_\alpha}^{(1)} u_\beta + S_{\alpha\beta}^{(1)} \partial_{x_\alpha}^{(1)} \rho \right] \right]$$

$$\text{(B-12)}$$

At last, the expression of g_i is derived as

$$g_i = g_i^{(0)} + \varepsilon g_i^{(1)} + \varepsilon^2 g_i^{(2)} + \cdots$$

$$= g_i^{(eq)} - \tau_g \Delta t \left[U_{i\alpha} C^{-1} g_i^{(eq)} \partial_{x_\alpha}^{(1)} C + 0.5 U_{i\alpha} C c_{i\beta} \partial_{x_\alpha}^{(1)} u_\beta - 0.5 \rho^{-1} C c_{i\beta} \partial_{x_\beta}^{(1)} p \right]$$

$$- \tau_g \Delta t \left[DC^{-1} g_i^{(eq)} \partial_{x_\alpha} \partial_{x_\alpha} C + 0.5 Y c_{i\beta} \rho^{-1} v \left[\rho \partial_{x_\alpha} \partial_{x_\alpha} u_\beta + S_{\alpha\beta} \partial_{x_\alpha} \rho \right] \right]$$

$$= g_i^{(eq)} - \tau_g \Delta t \left[U_{i\alpha} C^{-1} g_i^{(eq)} \partial_{x_\alpha}^{(1)} C + 0.5 U_{i\alpha} C c_{i\beta} \partial_{x_\alpha}^{(1)} u_\beta - 0.5 \rho^{-1} C c_{i\beta} \partial_{x_\beta}^{(1)} p \right]$$

$$- \tau_g \Delta t \left[DC^{-1} g_i^{(eq)} \partial_{x_\alpha} \partial_{x_\alpha} C + 0.5 C c_{i\beta} \rho^{-1} v \left[\rho \partial_{x_\alpha} \partial_{x_\alpha} u_\beta + S_{\alpha\beta} \partial_{x_\alpha} \rho \right] \right]$$

$$= g_i^{(eq)} \left[1 - \tau_g \Delta t C^{-1} (U_{i\alpha} \partial_{x_\alpha}^{(1)} C - D \partial_{x_\alpha} \partial_{x_\alpha} C) \right]$$

$$- 0.5 \tau_g \Delta t C c_{i\beta} (U_{i\alpha} \partial_{x_\alpha}^{(1)} u_\beta + v \partial_{x_\alpha} \partial_{x_\alpha} u_\beta + \rho^{-1} v S_{\alpha\beta} \partial_{x_\alpha} \rho)$$

$$+ 0.5 \tau_g \Delta t \rho^{-1} C c_{i\beta} c_s^{-2} \partial_{x_\beta}^{(1)} \rho \quad \text{(B-13)}$$

Eq. (B-13) is an analytic expression for the reconstruction of the concentration distribution function g_i from the macro concentration.

References

[1] A.A. Shah, K.H. Luo, T.R. Ralph, F.C. Walsh, Recent trends and developments in polymer electrolyte membrane fuel cell modelling, Electrochim. Acta 56 (11) (2011) 3731–3757.

[2] T.E. Springer, T.A. Zawodzinski, S. Gottesfeld, Polymer electrolyte fuel cell model, J. Electrochem. Soc. 138 (8) (1991) 2334–2342.

[3] D.M. Bernardi, M.W. Verbrugge, Mathematical model of a gas diffusion electrode bonded to polymer electrolyte, AIChE J. 37 (8) (1991) 1151–1163.

[4] D.M. Bernardi, M.W. Verbrugge, Mathematical model of the solid polymer-electrolyte fuel cell, J. Electrochem. Soc. 139 (9) (1992) 2477–2491.

[5] S. Basu, J. Li, C.-Y. Wang, Two-phase flow and maldistribution in gas channels of a polymer electrolyte fuel cell, J. Power Sources 187 (2) (2009) 431–443.

[6] L. Chen, T.-F. Cao, Z.-H. Li, Y.-L. He, W.-Q. Tao, Numerical investigation of liquid water distribution in the cathode side of proton exchange membrane fuel cell and its effects on cell performance, Int. J. Hydrogen Energy 37 (11) (2012) 9155–9170.

[7] Z.H. Wang, C.Y. Wang, K.S. Chen, Two-phase flow and transport in the air cathode of proton exchange membrane fuel cells, J. Power Sources 94 (1) (2001) 40–50.

[8] V. Gurau, J.A. Mann, T.A. Zawodzinski, Two-phase transport in PEM fuel cell cathodes, J. Fuel Cell Sci. Technol. 5 (2008) 021009-1–021009-12.

[9] A.D. Le, B. Zhou, A generalized numerical model for liquid water in a proton exchange membrane fuel cell with interdigitated design, J. Power Sources 193 (2) (2009) 665–683.

[10] W.Q. Tao, C.H. Min, X.L. Liu, Y.L. He, B.H. Yin, W. Jiang, Parameter sensitivity examination and discussion of PEM fuel cell simulation model validation: Part I. Current status of modeling research and model development, J. Power Sources 160 (1) (2006) 359–373.

[11] J.T. Gostick, M.W. Fowler, M.D. Pritzker, M.A. Ioannidis, L.M. Behra, In-plane and through-plane gas permeability of carbon fiber electrode backing layers, J. Power Sources 162 (1) (2006) 228–238.

[12] K.J. Lee, J.H. Nam, C.J. Kim, Pore-network analysis of two-phase water transport in gas diffusion layers of polymer electrolyte membrane fuel cells, Electrochim. Acta 54 (4) (2009) 1166–1176.

[13] J. Pauchet, M. Prat, P. Schott, S.P. Kuttanikkad, Performance loss of proton exchange membrane fuel cell due to hydrophobicity loss in gas diffusion layer: analysis by multiscale approach combining pore network and performance modelling, Int. J. Hydrogen Energy 37 (2) (2012) 1628–1641.

[14] T. Koido, T. Furusawa, K. Moriyama, An approach to modeling two-phase transport in the gas diffusion layer of a proton exchange membrane fuel cell, J. Power Sources 175 (1) (2008) 127–136.

[15] J.H. Nam, M. Kaviany, Effective diffusivity and water-saturation distribution in single- and two-layer PEMFC diffusion medium, Int. J. Heat Mass Transfer 46 (24) (2003) 4595–4611.

[16] J.W. Park, K. Jiao, X. Li, Numerical investigations on liquid water removal from the porous gas diffusion layer by reactant?ow, Appl. Energy 87 (2010) 2180–2186.

[17] G. Wang, P.P. Mukherjee, C.-Y. Wang, Direct numerical simulation (DNS) modeling of PEFC electrodes: Part II. Random microstructure, Electrochim. Acta 51 (15) (2006) 3151–3160.

[18] G. Wang, P.P. Mukherjee, C.-Y. Wang, Direct numerical simulation (DNS) modeling of PEFC electrodes: Part I. Regular microstructure, Electrochim. Acta 51 (15) (2006) 3139–3150.

[19] P.P. Mukherjee, C.-Y. Wang, Stochastic microstructure reconstruction and direct numerical simulation of the PEFC catalyst layer, J. Electrochem. Soc. 153 (5) (2006) A840–A849.

[20] J. Park, X. Li, Multi-phase micro-scale flow simulation in the electrodes of a PEM fuel cell by lattice Boltzmann method, J. Power Sources 178 (1) (2008) 248–257.

[21] L. Hao, P. Cheng, Lattice Boltzmann simulations of water transport in gas diffusion layer of a polymer electrolyte membrane fuel cell, J. Power Sources 195 (12) (2010) 3870–3881.

[22] P.P. Mukherjee, C.Y. Wang, Q. Kang, Mesoscopic modeling of two-phase behavior and flooding phenomena in polymer electrolyte fuel cells, Electrochim. Acta 54 (27) (2009) 6861–6875.

[23] L. Chen, H.-B. Luan, Y.-L. He, W.-Q. Tao, Pore-scale flow and mass transport in gas diffusion layer of proton exchange membrane fuel cell with interdigitated flow fields, Int. J. Therm. Sci. 51 (2012) 132–144.

[24] S.H. Kim, H. Pitsch, Reconstruction and effective transport properties of the catalyst layer in PEM fuel cells, J. Electrochem. Soc. 156 (6) (2009) B673–B681.

[25] J.A. Elliott, S. Hanna, A.M.S. Elliott, G.E. Cooley, Atomistic simulation and molecular dynamics of model systems for perfluorinated ionomer membranes, Phys. Chem. Chem. Phys. 1 (20) (1999) 4855–4863.

[26] A. Vishnyakov, A.V. Neimark, Molecular dynamics simulation of microstructure and molecular mobilities in swollen nafion membranes, J. Phys. Chem. B 105 (39) (2001) 9586–9594.

[27] W.Q. Tao, Y.L. He, Recent advances in multiscale simulation of heat transfer and fluid flow Problems, Prog. Comput. Fluid Dyn. 9 (3–5) (2009) 150–157.

[28] Y.L. He, W.Q. Tao, Multiscale simulations of heat transfer and fluid flow problems, ASME J. Heat Transfer 134 (3) (2012) 031018.

[29] H.B. Luan, H. Xu, L. Chen, D.L. Sun, W.Q. Tao, Numerical illustrations of the coupling between the lattice Boltzmann method and finite-type macro-numerical methods, Numer. Heat Transfer Part B Fund. 57 (2) (2010) 147–171.

[30] H.B. Luan, H. Xu, L. Chen, D.L. Sun, Y.L. He, W.Q. Tao, Evaluation of the coupling scheme of FVM and LBM for fluid flows around complex geometries, Int. J. Heat Mass Transfer 54 (2011) 1975–1985.

[31] L. Chen, H.-B. Luan, Y.-L. Feng, C.-X. Song, Y.-L. He, W.-Q. Tao, Coupling between finite volume method and lattice Boltzmann method and its application to fluid flow and mass transport in proton exchange membrane fuel cell, Int. J. Heat Mass Transfer 55 (13–14) (2012) 3834–3848.

[32] H.B. Luan, L. Chen, Y.-L. Feng, Y.L. He, W.Q. Tao, Coupling of finite volume method and thermal lattice Boltzmann method and its application to natural convection, Int. J. Numer. Methods Fluids 70 (2) (2012) 200–221.

[33] W.J. Zhou, H.B. Luan, J. Sun, Y.L. He, W.Q. Tao, a molecular dynamics and lattice boltzmann multiscale simulation for dense fluid flows, Numer. Heat Transfer Part B Fund. 61 (5) (2012) 369–386.

[34] Z.X. Sun, Z.Y. Li, Y.-L. He, W.-Q. Tao, Coupled solid (FVM)-fluid (DSMC) simulation of micro-nozzle with unstructured-grid, Microfluid. Nanofluid. 7 (5) (2009) 621–631.

[35] S.Y. Chen, G.D. Doolen, Lattice Boltzmann methode for fluid flows, Annu. Rev. Fluid Mech. 30 (1998) 329–364.

[36] Y.-L. He, Q. Li, Y. Wang, W.-Q. Tao, Lattice Boltzmann Method and Its Applications, Science Press, Beijing, 2009.

[37] P.L. Bhatnagar, E.P. Gross, M. Krook, A model for collision processes in gases. I. Small amplitude processes in charged and neutral one-component systems, Phys. Rev. A 94 (1954) 511–525.

[38] Y.H. Qian, D. d'Humiéres, P. Lallemand, Lattice BGK models for Navier–Stokes equation, Euro. Phys. Lett. 15 (1991) 603–607.

[39] S.P. Sullivan, F.M. Sani, M.L. Johns, L.F. Gladden, Simulation of packed bed reactors using lattice Boltzmann methods, Chem. Eng. Sci. 60 (12) (2005) 3405–3418.

[40] Q. Kang, P.C. Lichtner, D. Zhang, An improved lattice Boltzmann model for multicomponent reactive transport in porous media at the pore scale, Water Resour. Res. 43 (2007) W12S14.

[41] W.-Q. Tao, Numerical Heat Transfer, Xi'an Jiaotong University Press, Xi'an, 2001.

[42] D.L. Sun, Z.G. Qu, Y.L. He, W.Q. Tao, An efficient segregated algorithm for incompressible fluid flow and heat transfer problems – IDEAL (inner doubly iterative efficient algorithm for linked equations). Part I: Mathematical formulation and solution procedure, Numer. Heat Transfer Part B Fund. 53 (2008) 1–17.

[43] D.L. Sun, Z.G. Qu, Y.L. He, W.Q. Tao, An efficient segregated algorithm for incompressible fluid flow and heat transfer problems – IDEAL (inner doubly iterative efficient algorithm for linked equations). Part II: Application examples, Numer. Heat Transfer Part B Fund. 53 (2008) 18–38.

[44] Z.Y. Li, W.Q. Tao, A new stability-guaranteed second-order difference scheme, Numer. Heat Transfer Part B Fund. 42 (2002) 349–365.

[45] P. Albuquerque, D. Alemani, B. Chopard, P. Leone, A hybrid lattice Boltzmann finite difference scheme for the diffusion equation, Int. J. Multiscale Comput. Eng. 4 (2) (2006) 1543–1649.

[46] P.V. Leemput, C. Vandekerckhove, W. Vanroose, D. Roose, Accuracy of hybrid lattice Boltzmann/finite difference schemes for reaction-diffusion systems, Multiscale Model. Simul. 6 (3) (2007) 838–857.

[47] Q.S. Zou, X.Y. He, On pressure and velocity flow boundary conditions and bounceback for the lattice Boltzmann BGK model, Phys. Fluids 9 (6) (1997) 1591–1598.

[48] B. Alazmi, K. Vafai, Analysis of fluid flow and heat transfer interfacial conditions between a porous medium and a fluid layer, Int. J. Heat Mass Transfer 44 (9) (2001) 1735–1749.

[49] B. Goyeau, D. Lhuillier, D. Gobin, M.G. Velarde, Momentum transport at a fluid-porous interface, Int. J. Heat Mass Transfer 46 (21) (2003) 4071–4081.

[50] H. Meng, C.-Y. Wang, Model of two-phase flow and flooding dynamics in polymer electrolyte fuel cells, J. Electrochem. Soc. 152 (9) (2005) A1733–A1741.

[51] V. Gurau, J.A. Mann, Effect of interfacial phenomena at the gas diffusion layer-channel Interface on the water evolution in a PEMFC, J. Electrochem. Soc. 157 (4) (2010) B512–B521.

[52] A. Bazylak, D. Sinton, N. Djilali, Dynamic water transport and droplet emergence in PEMFC gas diffusion layers, J. Power Sources 176 (1) (2008) 240–246.